UNIVERSITY OF CRETE

DEPARTMENT OF MATERIALS SCIENCE AND TECHNOLOGY

Master thesis

Fraggelakis Fotis

Control of Ultrafast Laser – Surface Interactions Threw Polarization and Temporal Pulse Shaping

Supervisor:
P.A. Loukakos

Heraklion

February 2016

Contents

Abstract:

In this work we combine temporal pulse shaping and polarization conformation in order to control the ultrafast dynamical process which follows the excitation of a semiconductor surface by ultrashort laser pulses. Excitation of a semiconductor surface and further interference of the incident laser field with the surface wave leads to formation of a Surface Plasmon Polariton. The final product of this interference was found to be the creation of sub-wavelength periodic surface nanostructures, also known as ripples. The aim is to achieve control of the ripple characteristics. It was found that the symmetry, the period and the contrast of the ripples, strongly dependent on the temporal shape and the polarization of the incident laser pulses. Thus, we show that control and tuning of surface nanostructures can be achieved by controlling the ultrafast processes occurring on the semiconductor surface through utilization of non-standard laser-matter interaction methods.

Περιληψη:

Στην παρούσα εργασία συνδυάζουμε την τεχνική της χρονικής διαμόρφωσης παλμών (pulse shaping) και την τροποποίηση της πόλωσης με στόχο να επηρεάσουμε τις υπερταχείες διαδικασίες που ακολουθούν την οπτική διέγερση της επιφάνειας του πυριτίου με υπέρβραχείς παλμούς. Η διέγερση του ημιαγωγού και η συνεπαγόμενη συμβολή του προσπίπτοντος κύματος με την επιφανειακή ταλάντωση της πυκνότητας των ηλεκτρονίων (surface plasmon) οδηγεί στον σχηματισμό περιοδικών δομών στην επιφάνεια γνωστών και ως ripples. Στόχος μας ήταν να διερευνηθεί η δυνατότητα του έλεγχου των χαρακτηριστικών των ripples μέσα από την δι μόρφωση του χρονικού προφίλ και της πόλωσης του προσπίπτοντος παλμού. Στα πλαίσια της εργασίας , μέσα από μια σειρά πειραμάτων που διενεργήθηκαν στα πλαίσιά της ότι η συμμετρία, η περίοδος και η καθαρότητα των ripples, μπορούν να καθοριστούν μέσα από την χρήση μη συμβατικών μεθόδων αλληλεπίδρασης.

Introduction:

Surface nanostructuring has gained a lot of attention in the recent years. Femtosecond lasers made it possible to induce LIPPS in a various materials due to the high rate of energy deposition during irradiation. Many - photon absorption was the key to implement the previously studied nanostructure[2] to materials with band gap way larger than the irradiating photon energy.

From biomimetic surfaces[3] show in Figure 0.1 that can reproduce wetting properties such as super-hydrophilicity and super-hydrophobicity to materials that can drain liquids due to capillary flow[4] micro and nanostructured surfaces can exhibit fascinating properties in their interaction with liquids. These surfaces were a major advance in micro and nanofluidic devices, biochemical sensing, biomedicine.

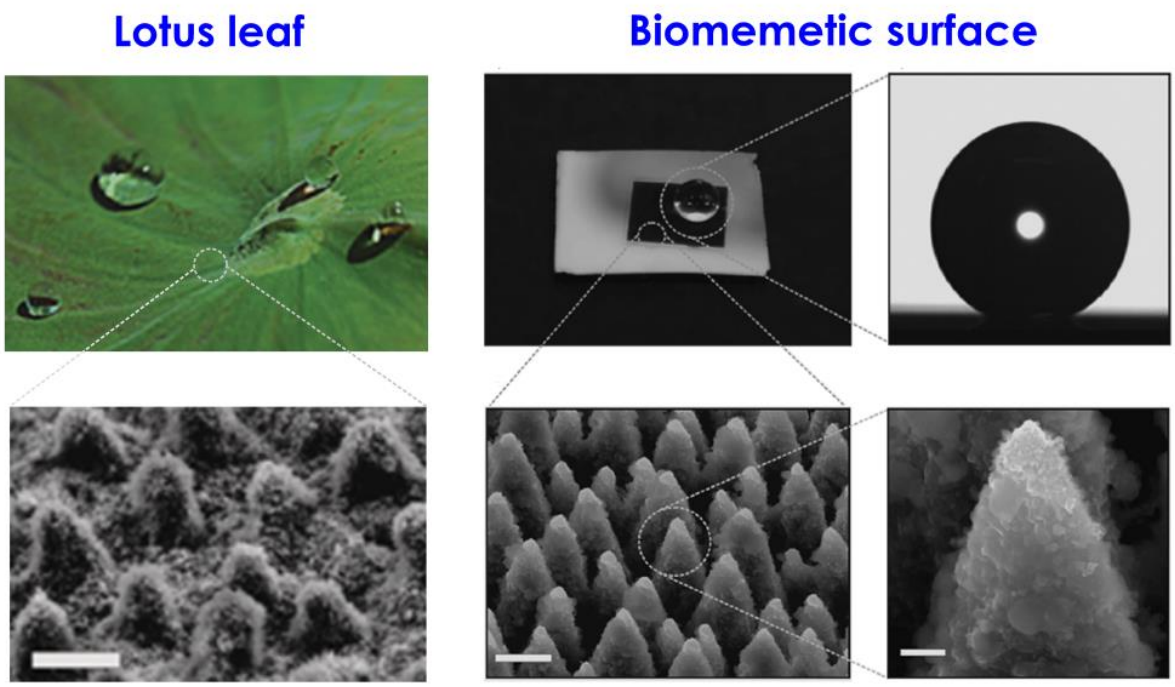

Figure 0.1 Nanostructured Materials Wetting Properties[3]

Optical properties of nanostructured surfaces must not be ignored. Many materials, dielectrics semiconductors and metals, exhibit altered absorbance and reflectivity compered to their untreated surface[5] as it is shown in Figure 0.2. Treated titanium can absorb efficiently visible and infrared light when treated. Also different kind of nanostructure can result in specified spectrum absorption and can make the surface appear with different color.

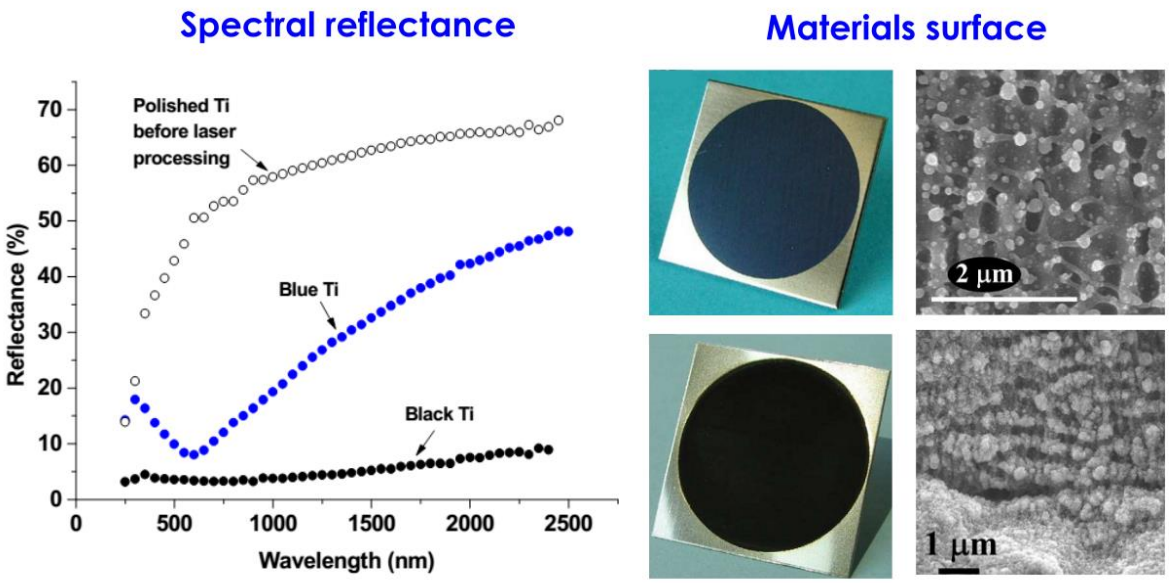

Figure 0.2 Nanostructured Optical properties (copy from [5])

It is well established threw many works that the resulting surface nanostructure can be determined, up to some point by controlling the irradiation parameters such as fluence, number of pulses and lasers wavelength. A small example of that statement is depicted in Figure 0.3 where different number of pulses can result in nanostructure with different morphology. Nevertheless this kind of determination of nanostructure morphology, lacks the ability to intervene with ultrafast processes, that undergo laser pulse irradiation.

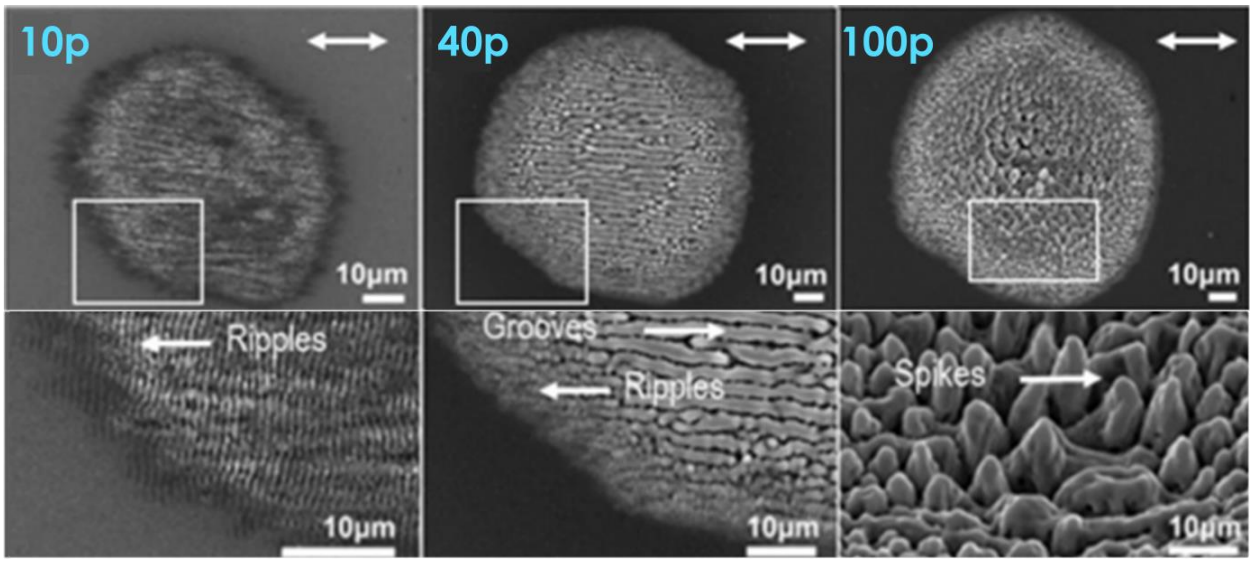

Figure 0.3 Nanostructured Silicon[6]

Pulse shaping – a way to create a sequence of pulses with variance of fluence and delay (Figure 0.4) - is a promising technique to overcome the aforementioned inability. Many studies have been focused in the influence of double pulse irradiation on surface interaction dynamics[7] more recently with the introduction of double crossed polarized pulses [8, 9] and dual wavelength double pulses[10], new methodologies were emerged to control the nanostructures morphology. This work aims to broaden this field of pulse shaping, presenting simple yet drastic ways to use double crossed polarized pulses in order to effect nanostructure orientation, period and morphology.

Figure 0.4 Pulse shaping

1 Interaction Mechanisms:

After the irradiation, the material undergoes several stages before it reaches an equilibrium state. For a typical direct band semiconductor, the various interaction processes do not occur sequentially but they overlap during the interaction forming a continuous chain of events. The overall procedure initiates with the photon absorption from the electrons and continues as that energy passes gradually to the lattice with electron phonon interactions, which – in the case in which sufficient energy is passed to the lattice- ablates, melts and then resolidifies. In semiconductors these procedures are categorized as shown in Figure 1.1 in four major regimes based on the timescale and the nature of interactions that each of those describes : (1) carrier excitation,(2) thermalization, (3) carrier removal and (4) thermal and structural effects[11].

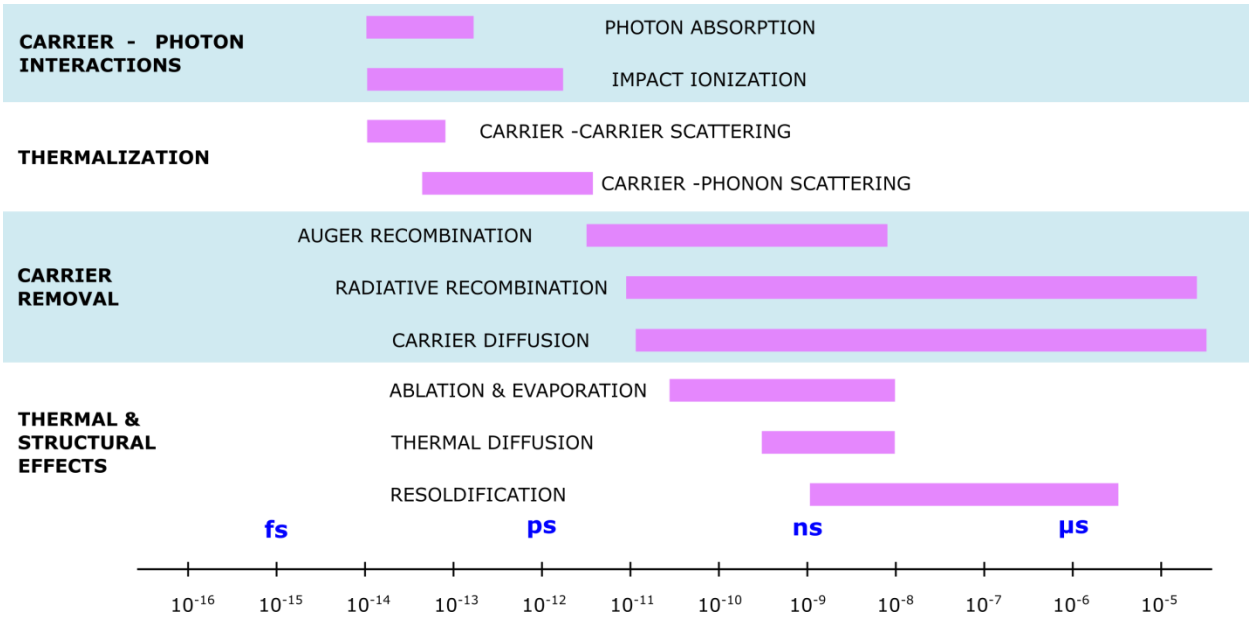

Figure 1.1 Ultrafast Interactions

After the irradiation of the surface with a single femtosecond pulse, a crater is formed as it is shown in Figure 1.2. This crater is the product of thermodynamical and fluid mechanical processes. In the following section a detailed examination of the dynamical proses will be presented.

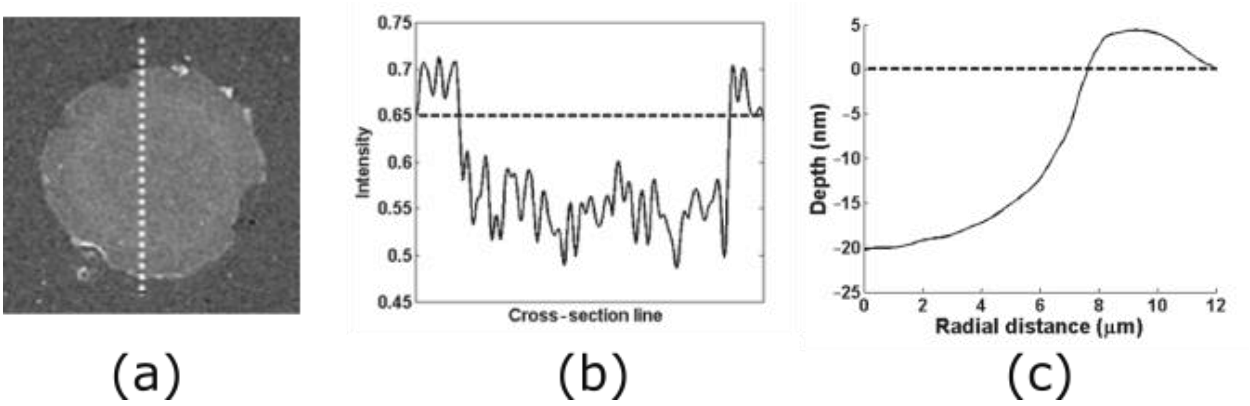

Figure 1.2 (Picture taken from Tsibidis et al. [1]) (a) SEM image of a crater (b) Cross section line of the intensity (c) Theoretical results for the depth of the crater

1.1 Ultrafast electron and lattice dynamics in semiconductors.

Soon after it was discovered that intense laser pulses of nanosecond duration from a ruby laser could anneal the lattice of silicon, it was established that this so-called pulsed laser annealing is a thermal process[1]. Although the radiation energy is transferred to the electrons, the electrons transfer their energy to the lattice on the timescale of the excitation for pulses that exceed picosecond duration. The electrons and the lattice remain in equilibrium and the laser simply 'heats' the solid to the melting temperature within the duration of the laser pulse. For ultrashort laser pulses in the femtosecond regime, however, thermal processes (which take several picoseconds) and equilibrium thermodynamics cannot account for the experimental data. On excitation with femtosecond laser pulses, the electrons and the lattice are driven far out of equilibrium [1](Figure 1.3) and disordering of the lattice can occur because the interatomic forces are modified due to the excitation of a large (10% or more) fraction of the valence electrons to the conduction band.

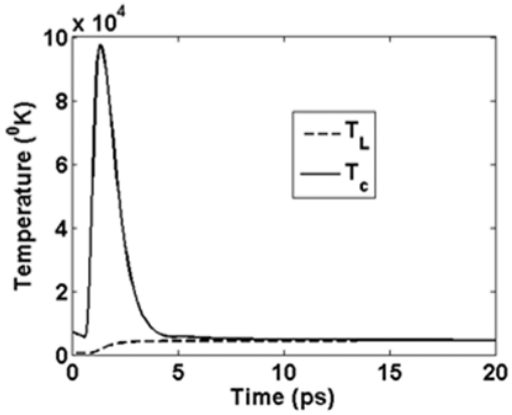

Figure 1.3 Simulation of electron & lattice temperature (Picture taken from Tsibidis et al. [1])

These procedures are analytically illustrated in the paragraphs below.

1.1.1 Carrier excitation

During the fs-laser irradiation of a semiconductor, if the photon energy is larger than the bandgap, single photon absorption (Figure 1.4a, left) is the dominant mechanism for exciting valence electrons to the conduction band. In the case of semiconductors with an indirect bandgap, such as silicon, single photon absorption can still occur with photons of energy greater than the gap, but phonon assistance is necessary to conserve momentum. Multiphoton absorption (Figure 1.4a, right) is important if the direct gap is greater than the photon energy, especially in transparent insulators, or if the single photon absorption is inhibited by band filling.

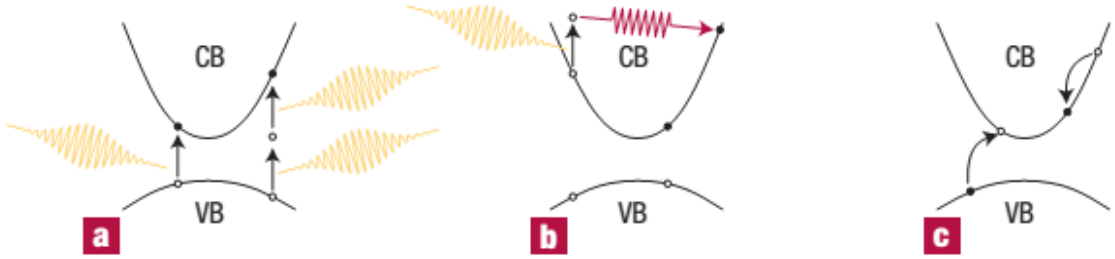

Figure 1.4 Carrier Excitation (Picture taken from Sundaram et al.[11])

Free carrier absorption (Figure 1.4b) increases the energy of carriers in the electron–hole plasma or that of the initially free electrons in a metal. Although this absorption increases the energy of the free carrier population, it does not alter its number density. However, if some of the carriers are excited well above the bandgap (or Fermi level in a metal), impact ionization (Figure 1.4c) can generate additional excited carriers.

1.1.2 Thermalization[11]

After excitation, electrons and holes are redistributed throughout the conduction and valence bands by carrier–carrier and carrier–phonon scattering. Carrier–carrier scattering (Figure 1.5a) is a two-body process (an electrostatic interaction between two carriers), which does not change the total energy in the excited carrier system or the number of carriers. During the duration of the femtosecond pulse the electrons reach a thermal equilibrium, in Figure 1.6 one can note the absence of a non thermal component in electron energy distribution at 120fs in silicon. In a carrier–phonon scattering process, free carriers lose or gain energy and momentum by emission or absorption of a phonon. This mechanism is responsible for the energy transfer from the electrons to the lattice. Because the emitted phonons carry little energy, it takes many scattering processes and therefore the interaction that lasts for several picoseconds. The carriers remain either in the same conduction or valence band valley (intravalley scattering, Figure 1.5b) or transfer to a different valley (intervalley scattering, Figure 1.5 c). Although carrier–phonon scattering does not change the number of carriers, their energy decreases due to spontaneous phonon emission, which transfers energy to the lattice. In metals and semiconductors, carrier–carrier and carrier–phonon scattering occur concurrently during the first few hundred femtoseconds after excitation.

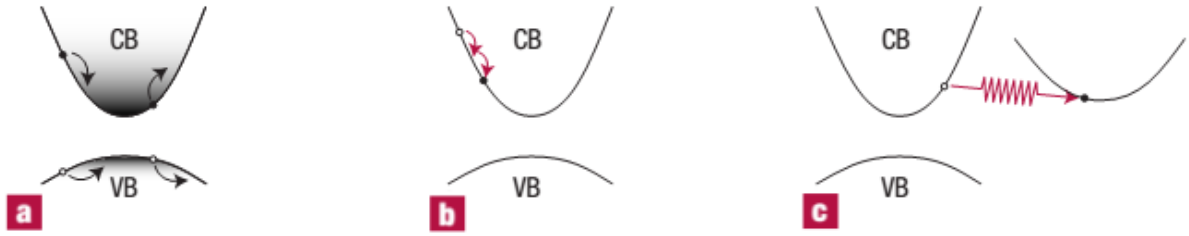

Figure 1.5 Thermalization (Picture taken from Sundaram et al.[11])

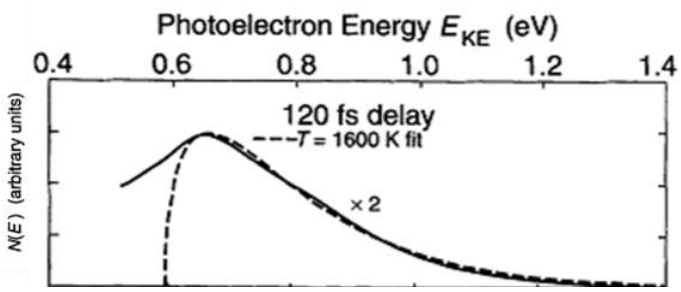

Figure 1.6 Electron temperature (image taken from Goldman et al.[12])

1.1.3 Carrier removal

Once the carriers and the lattice are in equilibrium, the material is at a well-defined temperature. Although the carrier distribution has the same temperature as the lattice, there is an excess of free carriers compared to that in the thermal equilibrium. The excess carriers are removed either by recombination of electrons and holes or by diffusion out of the excitation region. During radiative recombination, the inverse of the optical excitation process, the excess carrier energy is given up in the form of a photon (luminescence, Figure 1.7a).Non-radiative recombination processes include Auger recombination, and defect and surface recombination. During Auger recombination, an electron and a hole recombine and the excess energy excites an electron higher in the conduction band (Figure 1.7b). Like other recombination mechanisms, Auger recombination decreases the carrier density. However, it keeps the total energy in the free carrier system constant, and the average energy of the remaining carriers increases. In defect and surface recombination, the excess energy is given to a defect or surface state. Carrier diffusion removes carriers from the region of the sample where they were originally excited (Figure 1.7c) and so, in contrast to recombination processes, it does not decrease the total number of free carriers in the material.

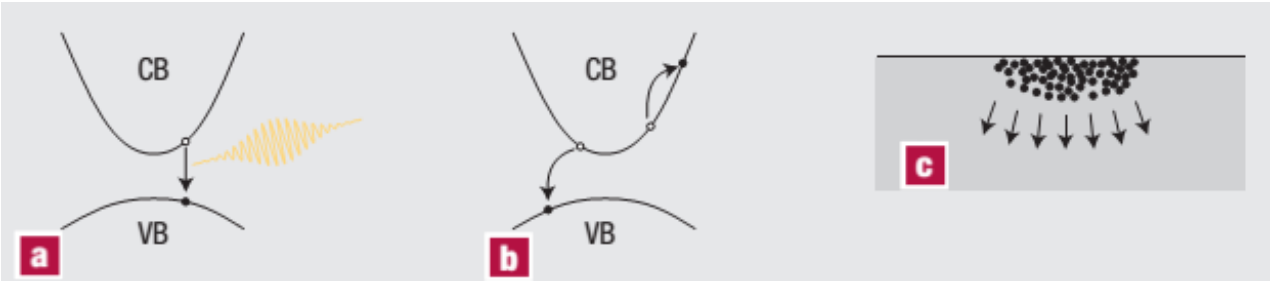

Figure 1.7 Carrier removal (Picture taken from Sundaram et al.[11])

In semiconductors, carriers are confined in the irradiated surface due to a decrease in bandgap on the excitation of a high carrier density[13], thus slowing down the diffusion away from the photoexcited region. This laser induced bandgap renormalization has been confirmed by theory as well as by experimental results[14]. For high fluences thus for large initial band bending the space charge layer can play a dominant role in governing carrier diffusion into the bulk, because it acts as a reservoir for photoexcited carriers. Recombination is suppressed in the reservoir because electrons and holes are separated. As it is show in Figure 1.8 nonequilibrium electrons and holes are formed into separated populations by the space charge layer's (SCL) electric field, and thus cannot recombine efficiently. This can enhance carrier density long after the bulk recombination time.[15] A surface photovoltage is created when photoexcited electrons and holes in the SCL separate to screen the surface charge responsible for the band bending.

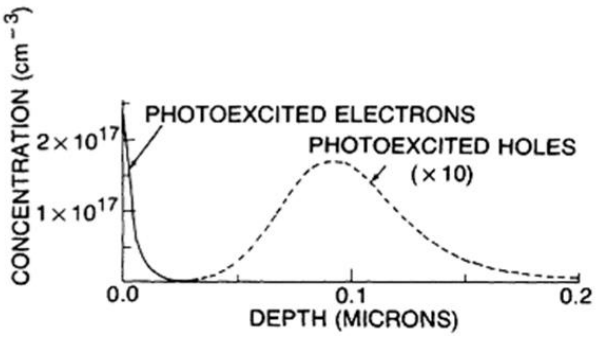

Figure 1.8 Nonequilibrium carrier densities 1 μs after the 100μJ/cm^2 laser pulse (Image taken from Long et al.[15])

1.1.4 Thermal and structural events

When the free carriers and the lattice come to equilibrium, the material is essentially the same as that heated by conventional means. Material excited by ultrashort laser pulses can achieve the equilibrium temperature in just a few picoseconds. If the lattice temperature exceeds the melting or boiling point, melting or vaporization can occur, but not on the picosecond timescale. The material is superheated but remains solid until regions of liquid or gas nucleate. Starting from nucleation sites at the surface, the liquid and/or gas phase expands into the material (Figure 1.9a). As the energy deposited by the laser pulse is converted to kinetic energy of the lattice ions, individual atoms, ions, molecules or clusters can leave the surface, leading to ablation (Figure 1.9b, that is, not thermal evaporation). In that case the material evaporates in small nm-scale bubbles that expand and force the material away of the surface[16, 17]. Thermal diffusion limits expansion of the liquid region by cooling the photoexcited region. If no phase transition occurs, the temperature reverts back to the ambient value on the timescale of microseconds. If melting or vaporization has occurred, then resolidification (Figure 1.9c) or condensation ensues as the temperature falls below the melting or boiling points, respectively; however ,the material does not necessarily revert back to its original structure or phase Figure 1.9 [18, 19] .

One aspect that should not be overlooked is that melting of silicon not only induces a solid-to-liquid phase transition but also alters its properties since the molten material exhibits metalic behavior. Hence, a revised two-temperature model that describes the heat transfer from electrons to lattice has to be employed[1] It is evident that the transition between a purely solid to a completely liquid phase requires the presence of an intermediate zone that contains material in both phases.

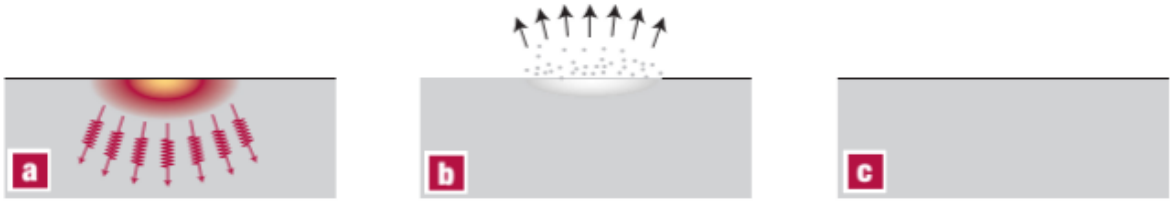

Figure 1.9 Thermal and structural effects (Picture taken from Sundaram et al.[11])

As it is previously discussed the decomposition process of the material depends strongly on fluence. In Figure 1.10 two examples calculated for different fluences are presented; (a) 750J/m^2 the material 50ps after irradiation starts to evaporate in small nm-scale bubbles under the surface and the material is ejected driven from their expansion and (b) 2000J/m^2 where the material evaporation starts in the surface leading to the ejection of small clusters. The fluence of the experiments presented in this work extends in even higher fluence regime.

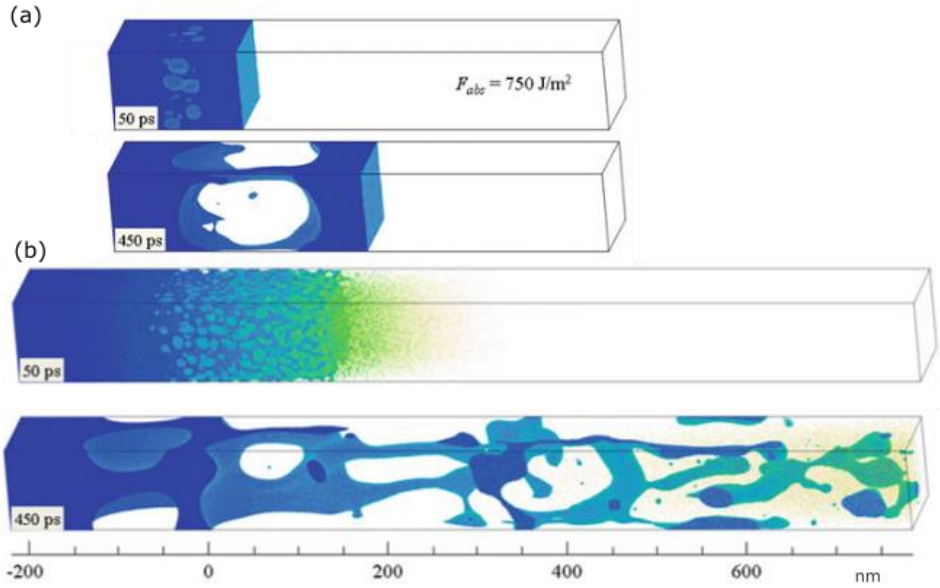

Figure 1.10 Ablation of a Solid (Simulation, taken from Chengpinget al.[17]) Shows the different was of evolution of an irradiated surface respectively with the fluence (a) F=750J/cm^2 (b) F=2000J/cm^2

Formation of the crater

After the material extraction threw ablation and evaporation, a crater is beginning to form due to variance of the depth of the ablation. The material that remains on the surface is treated as an incompressible Newtonian fluid. Figure 1.11 shows the Temperature spatial distribution of the irradiated material after 5ps. The material is divided into three regions: the first region (inside the region defined by the boundary in white) corresponds to material that is eventually evaporated because it reaches temperatures above that of $0.90T_{cr}$; the second one refers to a superheated liquid with temperatures in the range (T_m, $0.90T_{cr}$); the third region corresponds to material in solid phase with temperatures less than T_m.

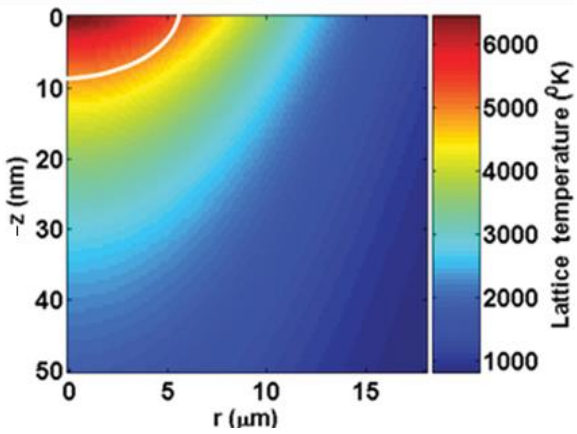

Figure 1.11 Temperature distribution (Picture taken from Tsibidis et al.[1])

(T_m = 1414 °C, T_{cr} = 4886°C)

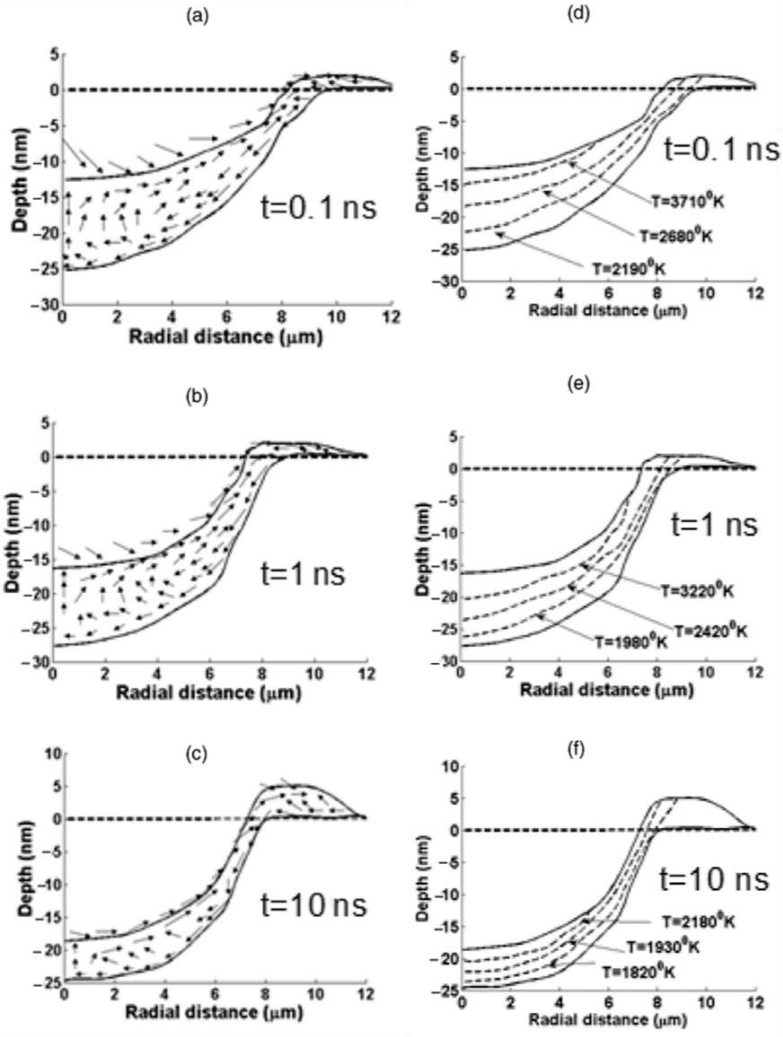

Figure 1.12 Crater Formation (Picture taken from Tsibidis et al.[1])

The resulting crater is a product of three dynamical movements of the molten material. In areas in which the material reaches the evaporation temperature vapor ejection creates a back (recoil) pressure on the liquid-free surface, which, in turn, pushes the melt away in the radial direction [20, 21]. The radial dependence of the temperature of the molten material due to the exponential profile of the laser beam leads to inhomogeneous surface tension which decreases as the radial distance increases this is an additional reason why liquid is pulled away from the center. That leads to further depression of the center of the crater. Moreover, the outward melt leads to the creation of a small protrusion at the edge of the affected region that undergoes melting whose curvature varies substantially with respect to the curvature of the surface closer to the beam center.

At later stages the resulting pressure will produce a protrusion whose size increases in a way that forces due to recoil pressure and surface tension will balance one another. [1] Figure 1.12 a-c illustrate the evolution and the transient behavior of the movement of the molten volume of the material, while the thick arrows show the direction of the associated velocity fields at t = 0.1ps, 1ps, and 10 ns, respectively. Recoil pressure initially has an important impact in the surface depression. Figure 1.12 show that molten material displacement due to the combination of recoil pressure and surface tension gradient results in a decrease of the melt thickness and melting of a new portion of the material. The temperature gradient coupled with surface tension gradient induces an outward and upward flow (i.e., Marangoni flow). Figure 1.12 d-f illustrate the temperature distribution at different timepoints, which is associated with the heat flow inside the molten material.

1.2 Ripple formation mechanism

Further irradiation of the nonplanar surface with a second pulse (which is performed after completion of surface solidification due to the first pulse) gives rise to a plasmon wave excitation that interferes with the incident field and produces a spatially modulated energy deposition[22] (Figure 1.13). Periodic temperature distribution along the modified surface again produces local surface tension gradients that, in combination with a balance between recoil pressure and surface tension pressure, are responsible for the rise and depression of the molten surface.

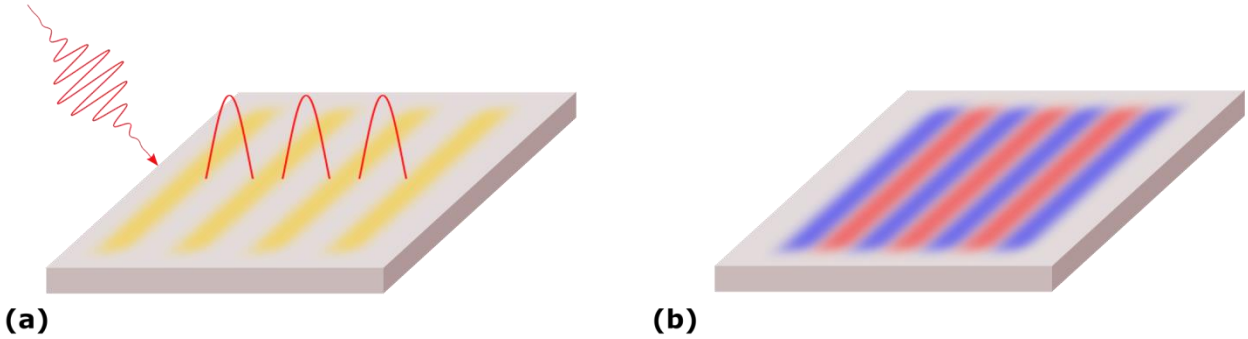

Figure 1.13 Surface Plasmon Polariton Interaction (a) interference of the incident pulse with the oscillating electron density (yellow) resulting in destructive and constructive interference(b) periodically heated surface (blue-cold, red-hot)

Surface plasmons

The involvement of a surface plasmon wave-related mechanism is proposed for the generation of ripples as the metallic behavior of silicon at high temperatures allows excitation of surface plasmon waves. Surface plasmon polariton, the coupling of the surface plasmon and the electric field, is excited

during the semiconductor irradiation due to the accumulation of free carriers [23] . The plasmon's wavelength, λs, is related to the wavelength of the incident beam through the relations [24]

Equation 1

$$\lambda_s = \left(\frac{\varepsilon' + \varepsilon_d}{\varepsilon' \varepsilon_d}\right)^{1/2}$$

$$\varepsilon' = Re\left(1 + (\varepsilon_g - 1)\left(1 - \frac{N}{n_0}\right) - \frac{N}{N_{cr}}\frac{1}{\left(1 + i\frac{1}{\omega\tau_e}\right)}\right)$$

where ε_d (ε_d = 1) is the dielectric constant of air, ε_g stands for the dielectric constant of unexcited material (ε_g = 13.46 + *i*0.048), ω is the frequency of the incident beam, and n_o is the valence-band carrier density (n_o = 5 × 1022 cm−3), and $N_{cr} = m_{eff}\varepsilon_0\omega^2/e^2$, where m_{eff} is the effective electron mass. [25]

The deposited laser intensity of the beam, due to the interference of the incident and the surface plasmon wave is estimated as shown in Equation 2.

Equation 2

$$I_{surf}(\vec{r}, t) = \langle\left|\vec{E}_i + n_{mat}\vec{E}_s\right|^2\rangle\, e^{-\left(\frac{2r^2}{R_0^2}\right)} e^{-4Ln2\left(\frac{t-t_0}{\tau_p}\right)^2}$$

Where n_{mat} is the refractive index of silicon, $E_i = E_{i,o}(r)\exp(-i\omega it + ik\,r)$ and $E_s = E_{s,o}(r)\exp(-i\omega st + ik_s \cdot r)$ and ω_i, ω_s are the frequencies of the incident beam (equal to ω) and the surface plasmon wave, respectively.

The magnitude of the electric field of the incident wave can be calculated by the expression;

Equation 3

$$\frac{E_d}{\tau_p} = \frac{c\varepsilon_0\sqrt{\pi}\,\langle\left|\vec{E}_i\right|^2\rangle}{2\sqrt{ln2}}$$

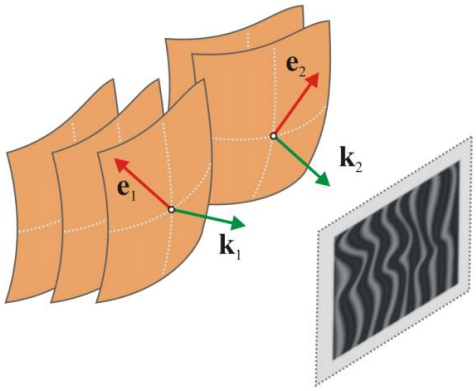

Figure 1.14 Interference of two polarized wave fronts (e_1 and e_2 represents the polarization of each wave and k_1 k_2 their wavevectors) Image taken from D.Papazoglou notes for Optics

while the magnitude of the electric field of the longitudinal surface plasmon wave [26] is taken to be of the order of the electric field of the incident wave. The computation of the time-averaged quantity in the final intensity on the surface Equation 2, yields a contribution proportional to $E_{i,o} \cdot E_{s,o.}$ This indicates that the polarization of the incident beam is crucial for the determination of the form of the total intensity distribution. Due to the curvature of the initially modified surface after irradiation with one laser pulse, the direction of the surface plasmon waves is geographically correlated.

Nevertheless, the energy deposition will be highest in the direction of the laser electrical field and lowest in the perpendicular direction because the electric field of the surface plasmon wave has a larger component along the polarization of the incident. Hence, the energy deposition is strongly correlated to the polarization of the laser beam, and it yields the highest component along the incident electric field polarization. As a result, for an incident beam with polarization on the xz the periodic function produces an optical interference pattern, which propagates in parallel to the polarization vector, and it is followed by a spatially and periodically modulated energy deposition.

This periodical energy deposition leads to the formation of ripples on the surface according to the fluidic dynamics described in Equation 2 Due to a periodic deposition of the laser density resulting from the interference of the initial beam with the surface plasmon, a recoil pressure will also be a periodic function and spatially modulated. Moreover, close to the points that are related to local minimum for the recoil pressure, the profile is characterized by an increased curvature that results in higher pressure due to surface tension. Hence, the collision of the two opposing types of pressures yields pronounced protrusions.

Figure 1.15 a-d illustrate the transient behavior of the movement of the molten volume and the distribution of the temperature fields after a second pulse irradiates the material (NP = 2) at t = 1 and 10 ns, respectively. Figures are restricted only to a small portion of the affected zone, equal to a 2.1-μm size along the x axis. The thick arrows in Figure 1.15 c & d show the direction of the associated velocity fields. Figure 1.15 e-f illustrate the periodic behavior of the spatial dependence of the recoil pressure at two different time points, t = 1 and 10 ns, respectively.

For irradiation with subsequent pulses, we note that the incident beam is not always perpendicular to the modified profile; therefore, the surface geometry influences the spatial distribution of the deposited

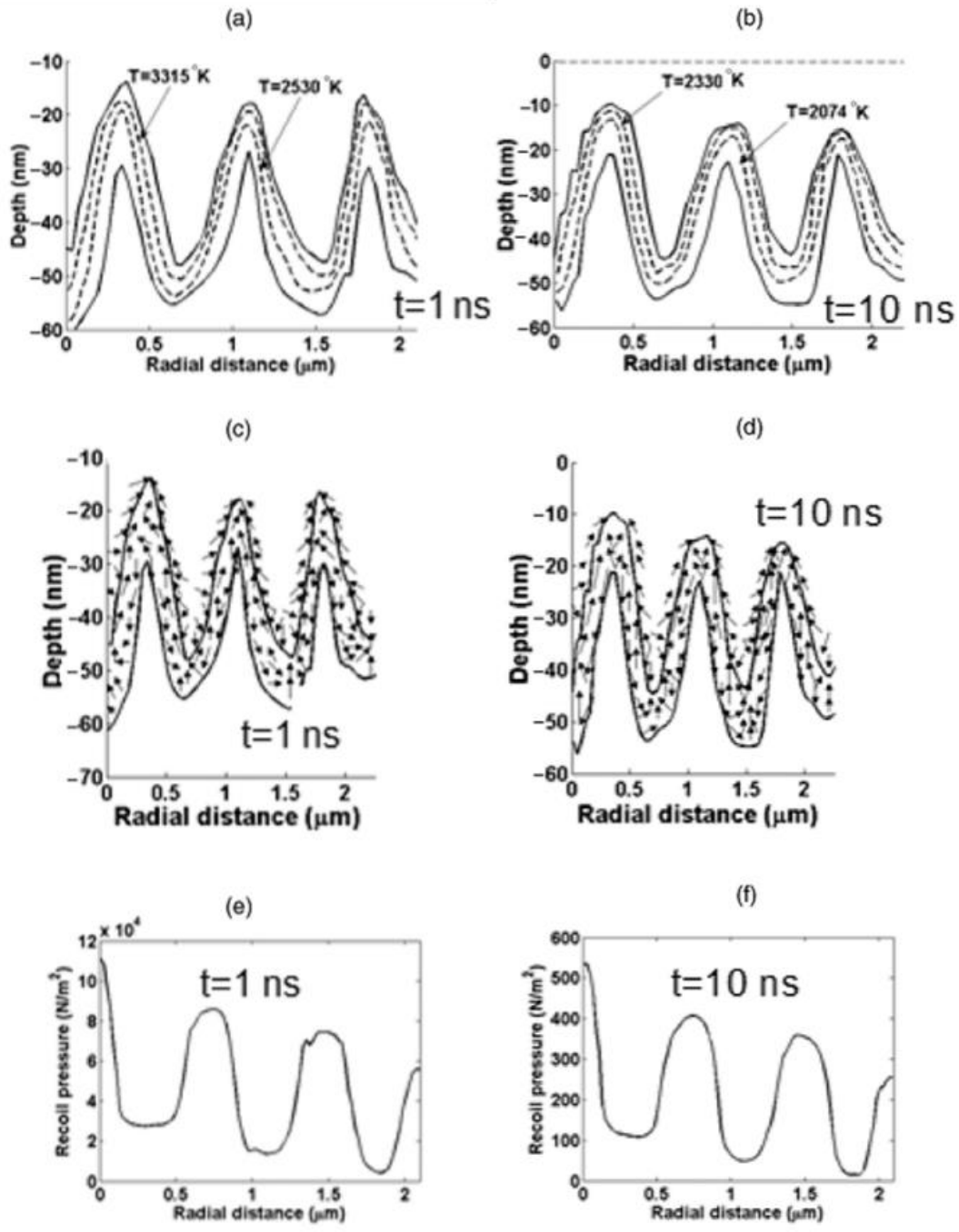

Figure 1.15 Ripple Formation (Picture taken from Tsibidis et al.[1])

laser energy. Hence, the laser irradiation reflected from the profile slopes can lead to light entrapment among the formed structures where the laser fluence is modified.

Figure 1.16 (a) illustrates the ripple formation for 2, 4, and 8 pulses on the xz plane at y = 0, and it is evident that the spot size, depth, and amplitude increase monotonically with the number of pulses. For NP = 4 ripples develop above the initial level of the surface profile (i.e., flat surface), while for smaller values of NP , ripples form below z = 0. Furthermore, a repetitive exposure to pulses leads to ripples with larger amplitude due to an increased gradient of energy deposition as the number of pulses grows, which causes the ripples to be more pronounced. Ripple height is spatially dependent due to the periodic variation of the gradient of the surface tension and temperature gradient that generates the creation of the periodic structures. Bigger variations are expected closer to the center of the laser beam, yielding structures with bigger peaks. The average ripple period after laser irradiation with four pulses at λ=800nm is estimated to be equal to 736 nm.

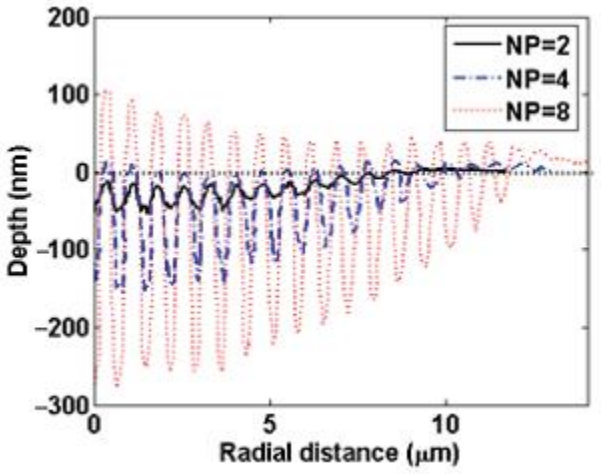

Figure 1.16 Progressive ripple formation (Picture taken from Tsibidis et al. [1])

1.3 Control of surface nanostructures using temporal pulse shaping

The previous paragraphs illustrate the formation of the simplest form of nanostructure, ripples, who's formation is observed in many materials upon femtosecond pulse irradiation. Despite the complexity of the presented process, the resulting morphology appears to be a deterministic result of the pulse characteristics such as duration, energy, polarization and wavelength. In this part we introduce a way to intervene to the sequence of ultrafast processes that follow the pulse excitation. That is temporal pulse shaping. The conformation of the fluctuations of the electric field in picosecond – timescale. Either by linear wave guiding[9] or by more sophisticated ways related with spectrum modulation[27] temporal pulse shaping is a research field of high interest in surface processing research[28] as also in the study of solid state dynamics.

Figure 1.17 Temporal Pulse Shaping

The simplest form of temporal pulse shaping is the creation of double pulses, where the temporal delay between the two is the experimental variable. In Figure 1.18 (a) electron temperature as a function of time upon double pulse irradiation with delay $5t_p$. The inset of Figure 1.18 a shows a sequence of two pulses forming a double femtosecond laser pulse with a temporal separation equal to 5tp between the two pulse components, where tp is the pulse duration (at FWHM) of each of the two pulses (b) the maximum temperature of electrons and the lattice for different delays (Ep = 0.24 J/cm2 per pulse, t_p = 430 fs, 800 nm laser wavelength). From Figure 1.18 we can clearly see the influence of double pulse delay in the way that the material (silicon) absorbs the energy of the pulse. Electrons reach higher temperatures for small delays but the lattice reaches its higher temperature at about 2ps delay. Thus electron energy is not efficiently transfer to the lattice for delays smaller than 2ps.[29]

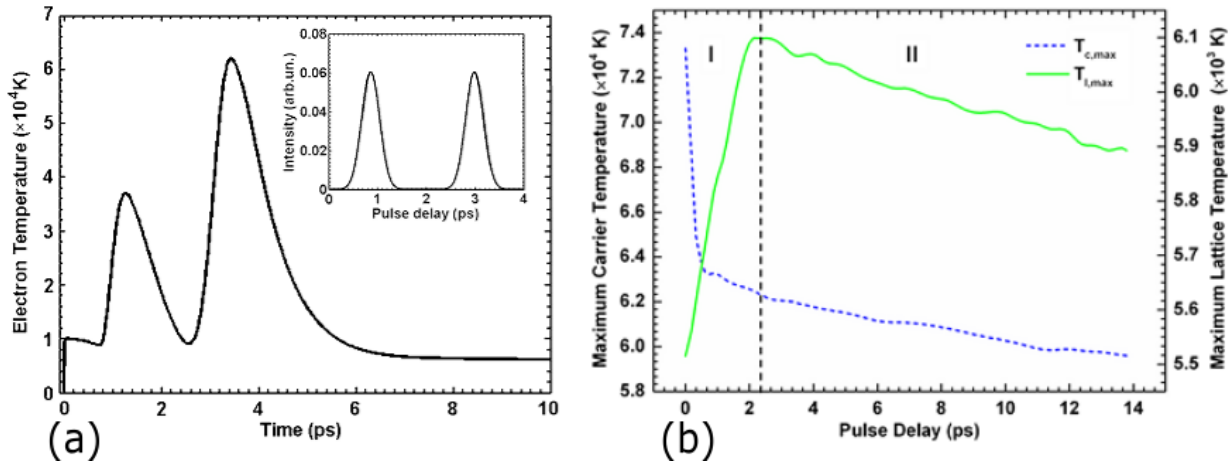

Figure 1.18 Double pulse Irradiation[30] (a)Evolution of Electron temperature upon double pulse irradiation, (b)Maximum electron and lattice temperatures in respect to double pulse delay

2 Background

Advances in the field of temporal pulse shaping established ways to control simultaneously temporal profile of a femtosecond pulse and its polarization[31, 32] (Figure 2.1). Taking into account the impact of polarization in nanostructure formation, polarization shaping in addition to and in parallel with temporal pulse shaping broadens the ability to control ripple formation mechanisms. Polarization shaping has been emerged as the state of the art along with the irradiation of the surface with subsequent pulses of different wavelength[10]. In the following paragraphs we present some results of those advances in order to introduce our own work in the field of Polarization and Temporal Pulse Shaping.

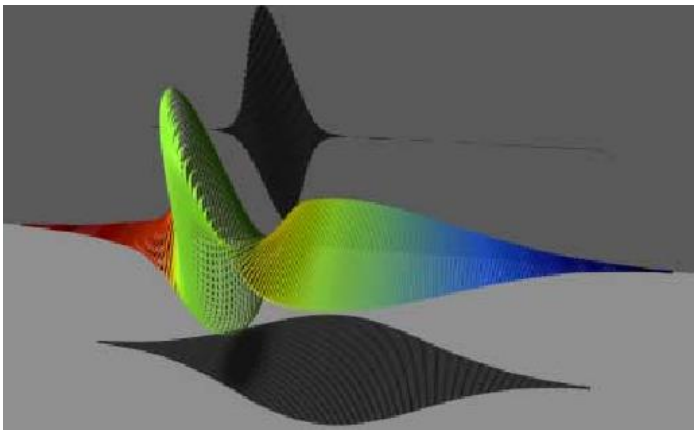

Figure 2.1 Polarization shaped pulse (picture taken from T. Brixner et al.[31])

2.1.1 Double pulses on semiconductors and dielectrics

Ripple periodicity, a factor strongly correlated to surface interaction dynamics and more specifically to the density of the carriers. It was found to alter as the number of pulses increases in semiconductors [1] [33] (Figure 2.2).

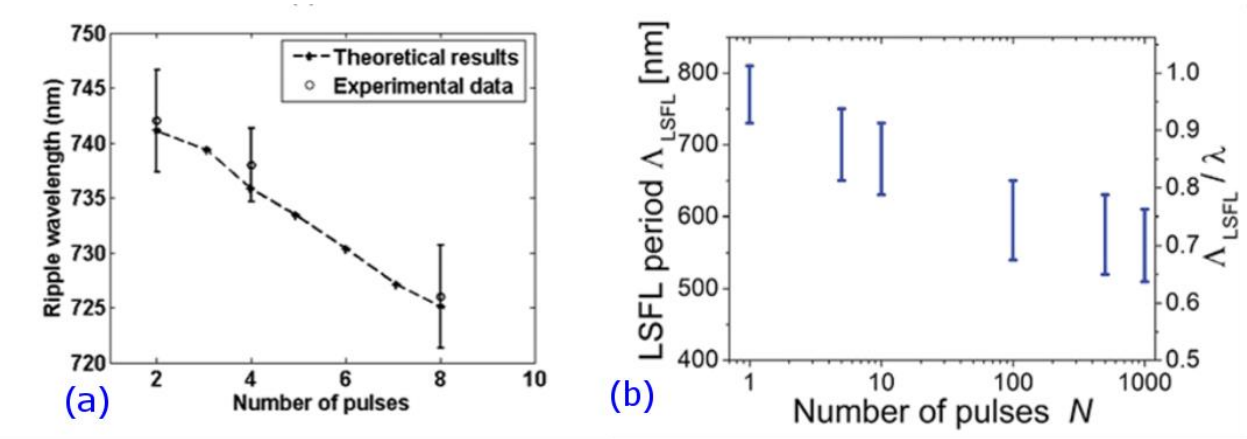

Figure 2.2 Modified Copy From [1](a) [33] (b) Ripple dependency to the number of pulses

Double pulse experiments in ZnO gave evidence that there is a strong correlation of the ripple periodicity to the pulse delay. More specifically it was found that for delays larger than 500fs between the pulses the ripples shift in crystalline ZnO from low frequency ripples to medium and high frequency ripples as it is shown in the figure below [7]:

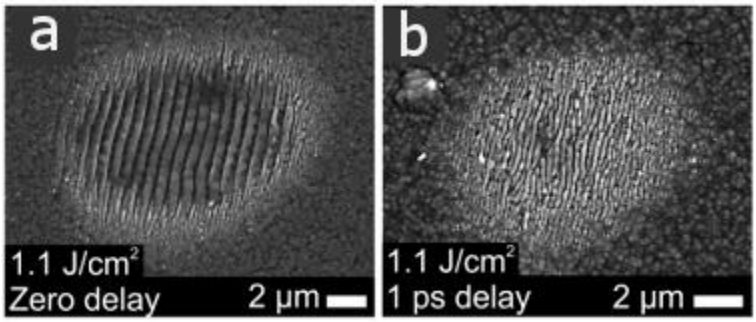

Figure 2.3 Ripple periodicity shift (modified image taken from Barberogloy et al. [7])

The creation of HF ripples was observed in many materials and it is related to double photon absorption in single pulse irradiation [34], also the change of refractive index is proposed for the creation of HF ripples[35].

2.1.2 Crossed polarization double pulses

An advance in the implementation of pulse shaping for surface processing application has been done with the introduction of a modified autocorrelation setup that could modify both time delay and polarization[8]. The experiment covered the time-delay window from -20ps to 20ps. The result of the irradiation is that the first pulse is the one that has greater impact in the orientation of the induced nanostructure as it can be seen in the figure below(Figure 2.4). The fact applies even if the energy of this first pulse is smaller than the second's, although the strongest laser pulse of the pair can define the LSFL orientation at large pulse delays in the ps-range. Also a decrease of the LIPPS wavelength was observed for an increase of the delay in picosecond-timescale[8].

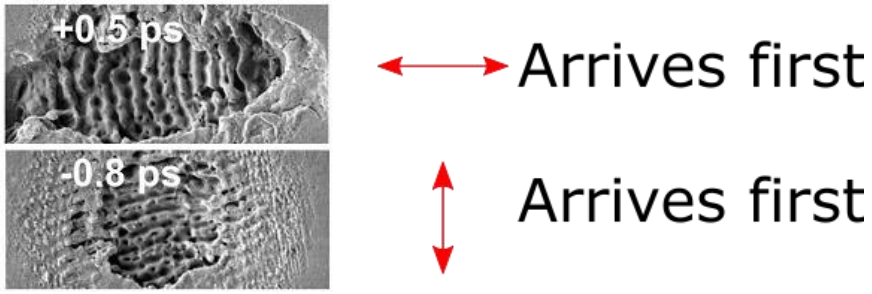

Figure 2.4 Ripple orientation dependence to the pulse row (Modified image taken from Rollhof et al. [8])

Experiments which include temporal and polarization pulse shaping where performed also in silicon[9] but they do not focus in small number pulse irradiation which we will present. The fragile information imprinted on the surface fades as the number of pulses increase. In our experiment we have irradiated the surface with two sets of double pulses in order to revile the influence of polarization shaping in the interaction dynamics. Moreover we aimed to the detailed examination of small delays (below 500fs) as also in the delay region in which the two crossed polarized pulses overlap.

3 Experimental Details:

3.1 Laser System

The source that was used for the experimental process is a FEMTOPOWER™ COMPACT™ PRO kHz-repetition rate, multi-pass titanium-sapphire amplifier which is seeded by a broadband femtosecond pulses from a mirror-dispersion controlled titanium-sapphire oscillator and uses a modified version of the chirped-pulse-amplification scheme.

This laser system is based on a Spectra Physics Tsunami oscillator, which delivers 80-100 fs pulses at a repetition rate of 81 MHz with a power of 500 to 600 mW and a FWHM of 10 nm. The pump laser used for this system is a Spectra Physics Millenia Nd:YLF, which pumps the oscillator with a power of 5 W. A ―Thales Laser System‖ (stretcher, amplifier, compressor) amplifies the beam by using another Ti:Sapphire crystal and a 12 W Q-switched Nd:YLF pump laser (B. M. Industries). During the chirped pulse amplification the repetition frequency is lowered from 81 MHz to 1 kHz by a pulse picker (pockels cell) inside the cavity of the amplifier. After being amplified the pulse is linearly polarized, it has a length

of 180 fs with a repetition rate of 1 kHz and a power of 500 to 600mW, respectively. After amplification the pulses are recompressed to less than 40 fs by a prism compressor.

3.2 The Setup

The setup that was used to accomplish the experiments is shown in (Figure 3.1)

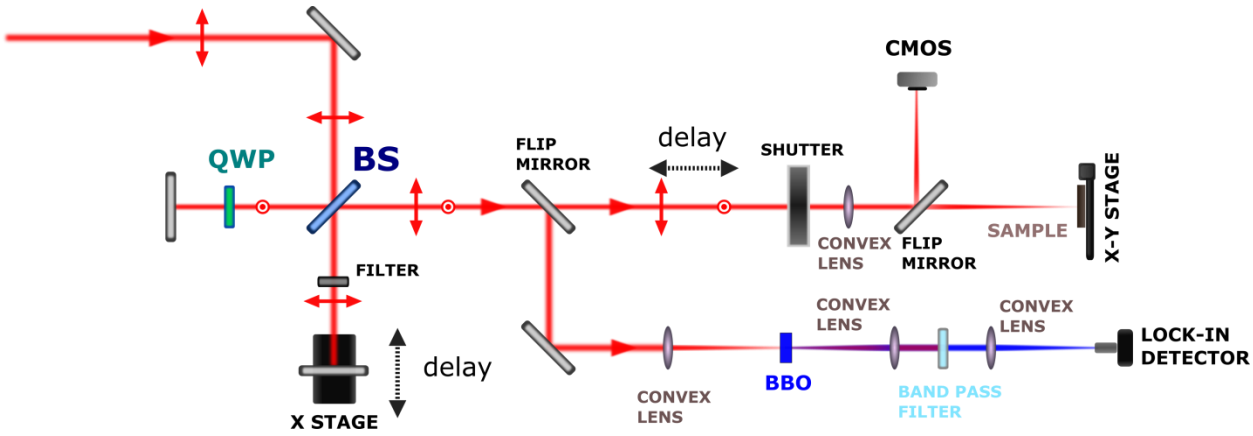

Figure 3.1 The Setup

The setup consists of three parts:

3.2.1 The modified autocorelator

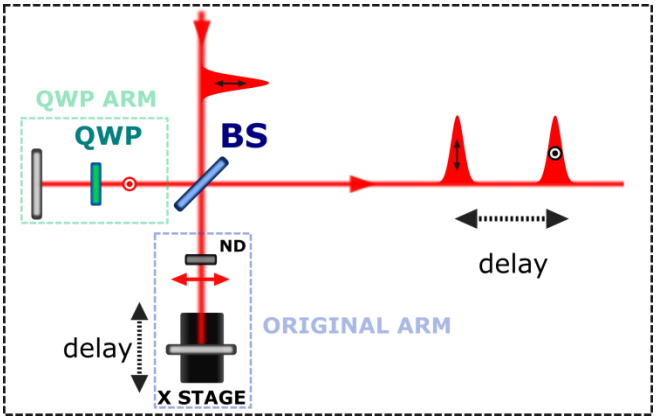

Figure 3.2 The modified autocorelator

This part (Figure 3.2) of the setup is used to create two subsequent pulses with crossed polarization and controllable time delay between them. Time delay can vary from -80ps to 80ps (relatively to the vertically polarized pulse) with accuracy of 0.2fs.

- Original Arm (OA)

A motorized, one-axis translation stage (50 mm (1.97") Low-Profile Motorized Translation Stage) was used in order to control the delay between the pulses. A neutral density filter was used to adjust the energy of the horizontal polarized pulse.

- QWP Arm (QA)

Here, a quarter wave plate (QWP) was introduced in the beam path in order to convert the polarization to circular in the first passage and at the second to convert t again to linear polarizes pulse oriented at 90^{O}respectively to its initial axis.

3.2.2 The characterization Part

In order to define the delay between the pulses and the temporal profile of the pulse, a characterization was built in the setup. A flip mirror is inserted in the beam path as it is show in the scheme (Figure 3.3) in order to guide the beam to the sensor.

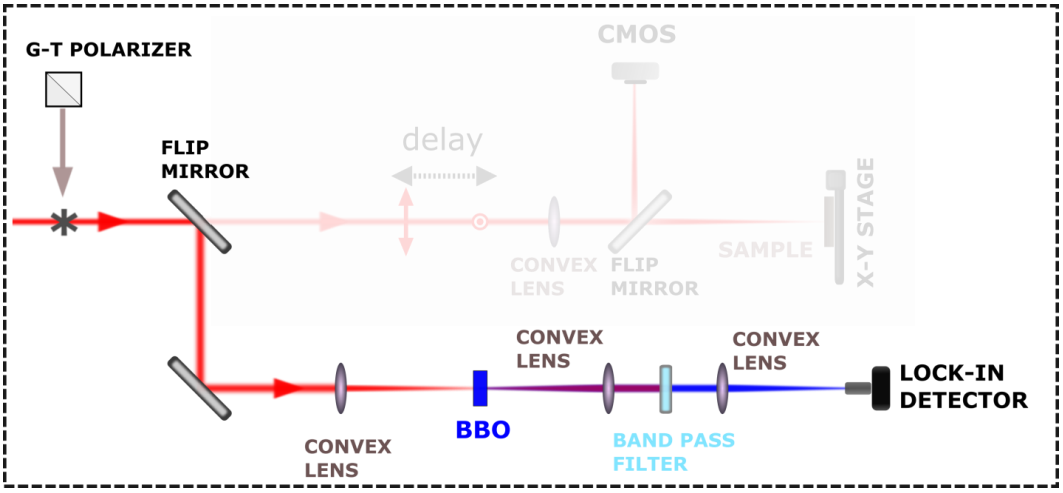

Figure 3.3 The characterization part of the setup

The beam is focused inside a 100µm thick BBO crystal that converts a part of the beam to its second harmonic and after that a set of lenses focuses the beam in to a photodiode that is connected to a lock in amplifier. Between the two convex lenses, a band pass filter it is placed to cut off the fundamental laser wavelength (785nm).

In order to measure the field correlation a Glan-Thomson polarized was placed as it is shown in Figure 3.4. Using this setup it was able to measure the meeting point of two pulses by measuring the projection along G-T optical axis when the two pulses are added in phase (defined as the maximum projection along the G-T OA) or out of phase (defined as the maximum projection in 90^{o} respectively to the G-T OA)

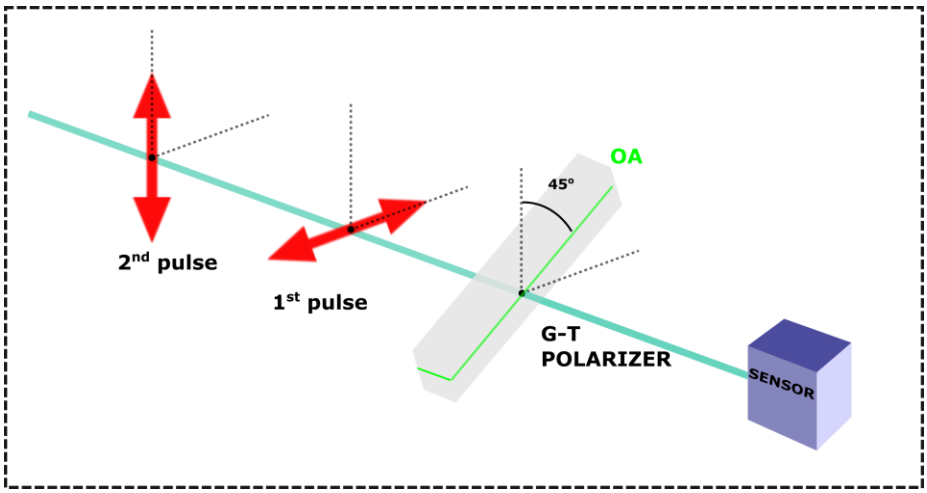

Figure 3.4 The setup used to measure the correlation of two crossed polarized pulses

3.2.3 The Surface Irradiation Part

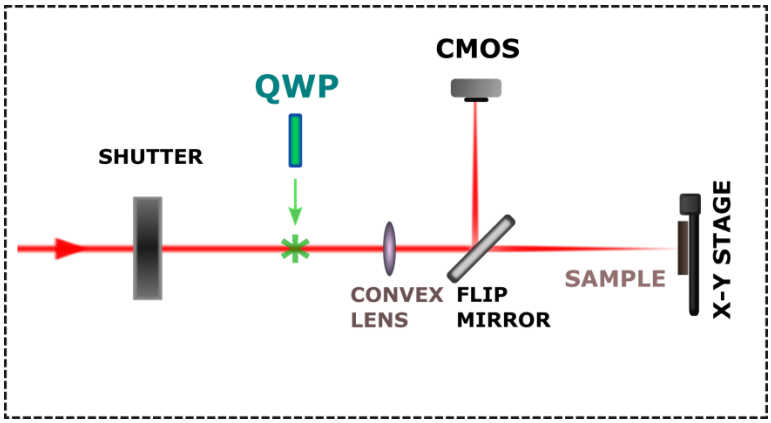

Figure 3.5 The irradiation part

A shutter was implemented in order to use the optimal number of pulses in the surface. An X-Y motorized stage was used to move the sample towards the beam.

The samples used were single crystal n-type Si(100) wafers with a resistivity of 2-8 Ohm from

3.3 Analysis Methods:

3.3.1 2D Fourier Transform Image analysis

In order to make accurate measurement of the ripple periodicity and its dispersion the obtained (scanning electron microscopy) SEM Images were transformed into Fourier space images. The exact procedure of the transformation and analysis is presented in the following paragraphs.

3.3.1.1 Transform of the SEM Image

In order to extract spatial symmetry information as well as to make precise measurements 2D FFT transform was utilized. An algorithm has been developed in order to perform the following procedures in the selected images (Figure 3.6):

1. Remove image labels that were inserted by the SEM software.
2. Perform 2D FFT transform in the complete image in order to get the information about all the possible frequencies that are present in the nanostructured spot.
3. Crops the image to the optimal size for observation

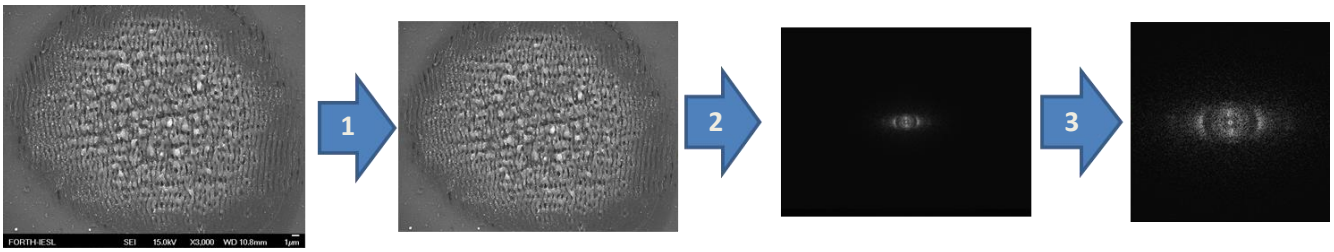

Figure 3.6 2D Furrier transform of an image

3.3.1.2 Fourier Space

The transformation changes the images dimensions as it is shown in the Figure 3.7. The dimensions of the generated fourier image (Figure 3.7 b) are inversely proportional to x and y dimensions of the initial image. The orange axis (Figure 3.7 a&c) represents the direction vertical to the ripple nanostructure. Along this axis the Fourier transformation detects a periodical fluctuation of the images intensity (Figure 3.7 a&c). This fluctuation has an average frequency and dispersion the length of this frequency is inversely proportional to the average ripple period. In image Figure 3.7 d one can note the major symmetry axis of the image present in the 2D Fourier Transformed image.

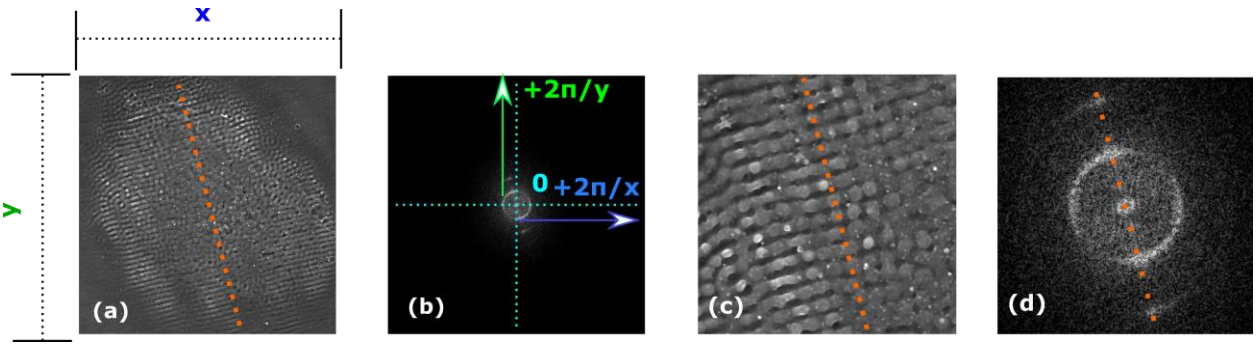

Figure 3.7

3.3.1.3 Measurement of Ripple period

In Figure 3.8 we present an example of ripple period measurement. Figure 3.8 b is the 2D Fourier transform of the image shown in Figure 3.8 a. Starting from the center of the image (zero), a vector pointing to the brightest marks of each regime(Figure 3.8 b) represents the most intense frequencies detected in the initial image (Figure 3.8 a). Low frequency ripple period is inversely proportional to the length of the red vector (shown in Figure 3.8b) and high frequency ripples are inversely proportional to the length of the blue vector. Each of the vectors show also the direction of the frequency detected on the initial image. Finally an example of HF ripples is presented in Figure 3.8 c (detail from Figure 3.8 a).

HF ripples in this image are less intense compered to LF ripples so their frequency intensity is lower in the 2DFT image.

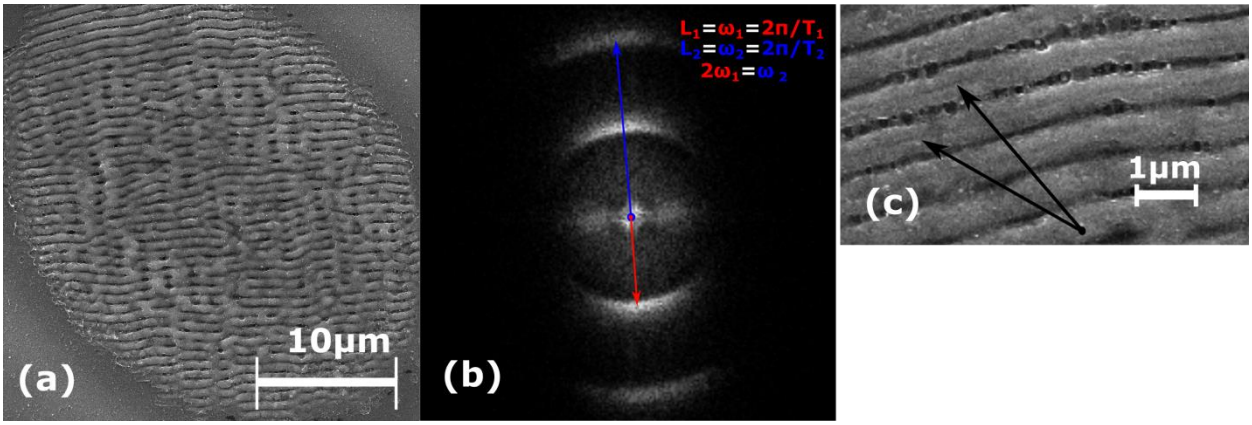

Figure 3.8 (a) sem image (b) Low frequency ripples (red vector) and High Frequency ripples (blue vector) represented in Fourier transformed image (c) HF ripples

The 2DFT image is converted as a matrix and stored into an image file, a measuring procedure is performed as described below.

- In each direction the program measures the average vertical value of 10 lines parallel with the studied axis
- In the resulting 1D matrix the program find the position of the maximum for each area. That position represents the central frequency of the ripple period in the inverse space.
- Another part of the program performs a Gaussian fitting in that area in order to extract an accurate measurement of the dispersion of the central frequency.

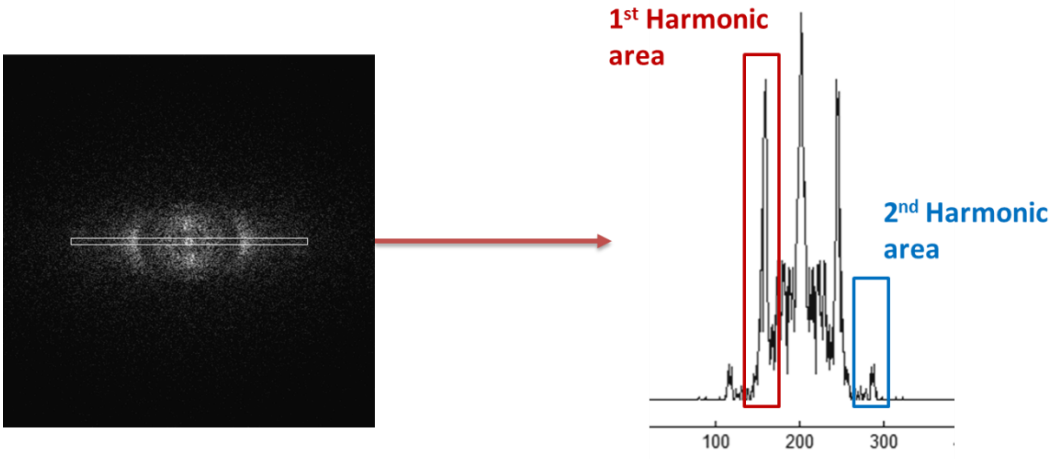

Figure 3.9

The normalization in the presented graphs refer to the ratio of the intensity of the measured peek divided by the summation of the intensities of the peeks in both axes:

$$I_n = \frac{I_{x\ or\ y}}{I_x + I_y}$$

3.3.1.4 Statistical Analysis

In all of the cases the graphs that are shown are the product of statistical analysis of many images. As described above the obtained frequency value as also the wideness of frequency distribution is transformed in period by taking into account the furrier space dimensions. Those values are afterwards subjected to statistical analysis and the average value for each measurement and its standard deviation were obtained.

3.3.1.5 Average 2D FFT image

Another analysis method that was used in order to present dense information in a single image, is the averaging of the values of many 2D FFT images that come from SEM images from iterations of the same parameters. The 2D FT images are merged into one 2D FFT image as shown in Figure 3.10.

Eg For the obtained image I from k images (I_k) that are iterations of the same conditions:

$$I(i,j) = \frac{1}{n}\sum_{k=1}^{n} I_k(i,j)$$

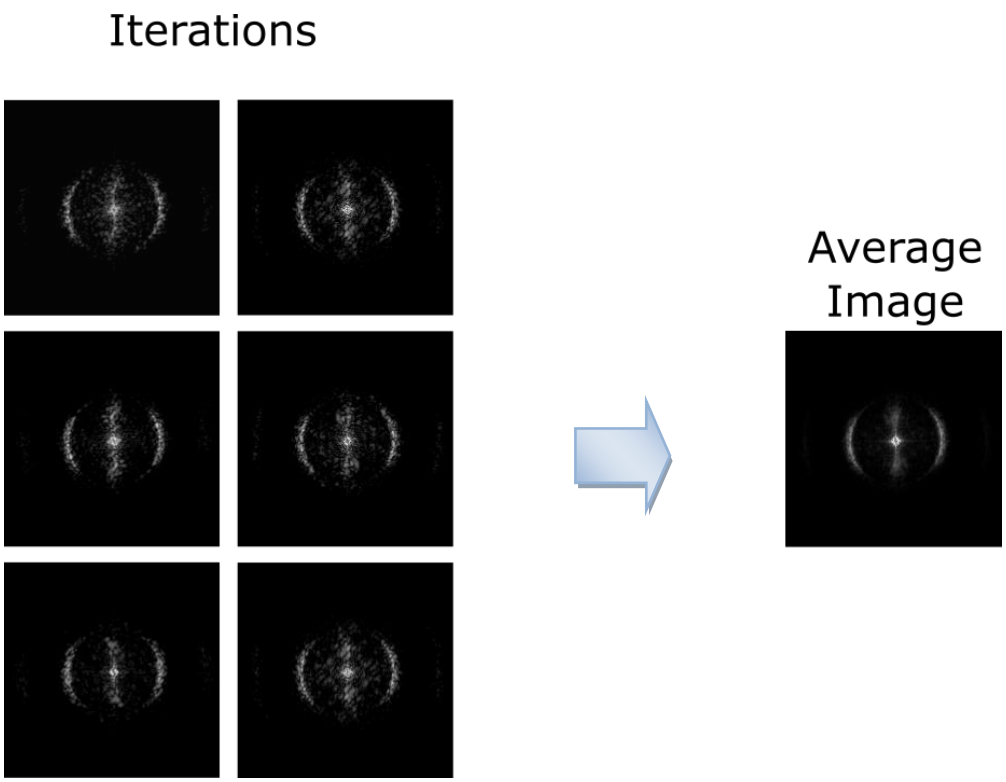

Figure 3.10 Averaging of a Fourier Image

3.3.2 Fluence Calculation

An important parameter that can define the induced nanostructure on the surface is fluence. Fluence is the energy per pulse per square centimeter in some cases or per square meter in others. Here we will use the first definition (J/cm^2) in order to characterize the irradiation conditions (Equation 4).

Equation 4

$$F = \frac{energy\ (J)}{A\ (cm^2)}$$

In order to estimate the fluence an image was taken with a CMOS camera at the focus of the laser beam. From the two dimensional Gaussian fit of this image the two waists of the ellipse of the resulting curve are extracted as it is shown in Figure 3.11.

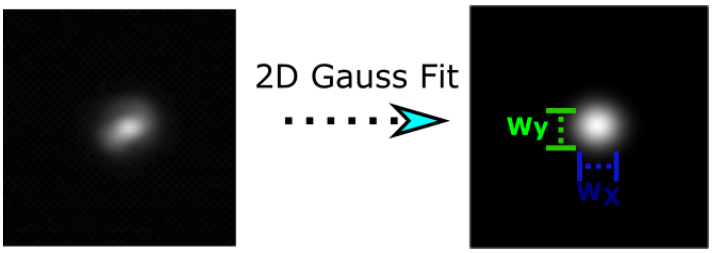

Figure 3.11

After the extraction of the wastes wx and wy from the Gaussian Fitting, the total area is calculated with the following equation

$$A = \pi \frac{w_x}{2} \frac{w_y}{2} \cdot (Camera\ scale)$$

4 Experimental Results & Discussion

In this part we present the way to modify the silicon surface in a controlled way. In all the presented examples two sets of two crossed polarized pulses were used to irradiate the surface. A set of pulses refers to two subsequent crossed polarized pulses and from now on the number of sets will be referred as N. The delay between the pulses of the set varies in from -50 ps to 50 ps. The sign indicates the order of the arrival of the pulses, where negative means that the pulse which is polarized along the y axis is the leading pulse and positive indicates the opposite. Two subsequent sets of pulses are separated by 1 ms which is the inverse of the laser system repetition rate. This time is sufficient for the surface to return to the thermodynamic equilibrium state as before excitation.

The observations of the influence of the time delay were not profound if the number of sets increases above 4 or 5 ($N > 4$ or $N > 5$). The clearness of the induced nanostructures for these cases urged us to present only the data obtained for $N = 2$.

Fluence was a major parameter. The total fluence for the two pulses was kept very close to the material's damage threshold. Great care was expended in order to keep the fluence distribution between the two pulses as equal as possible. Similarly, the spatial profiles of the two beams were kept as similar as possible. However, small deviations still existed resulting in slight differentiation of the two spatial beam profiles at the beam focus. This has been attributed to the fact that:

- The two pulses are passing through different optics in order to modify their energy and polarization and so there were some minor unavoidable differences in their profiles at the focus. An example is given in Figure 4.1.
- The allocation of the fluence. As it will be further discussed the fluence of each of the two pulses plays a key role in the predominance of each nanostructure orientation, and the energy distribution along the surface must be equal for the two crossed polarized pulses in order to reduce the effects on the surface morphology that are related to the energy distribution inequality. This experimental condition couldn't be totally satisfied.
- The polarization contrast. That is the ratio of the polarization along the major polarization axis respectively to its orthogonal axis. The pulse that passes twice along the QWP is inevitably stretched due to the GVD and also it won't be 100% linearly polarized due to the finite spectral width.

Despite the above difficulties, through careful determination of the other more controllable parameters, experimental results of high quality were obtained.

4.1 Cross-polarized pulses with equally distributed fluences

For experiments that are presented in paragraphs 4.1.1 (Large Delays) and 4.1.2 (Intermediate Delays) the induced nanostructures of single arm irradiation (QWP arm & Orig arm) are presented in Figure 4.1 for two different fluences each.

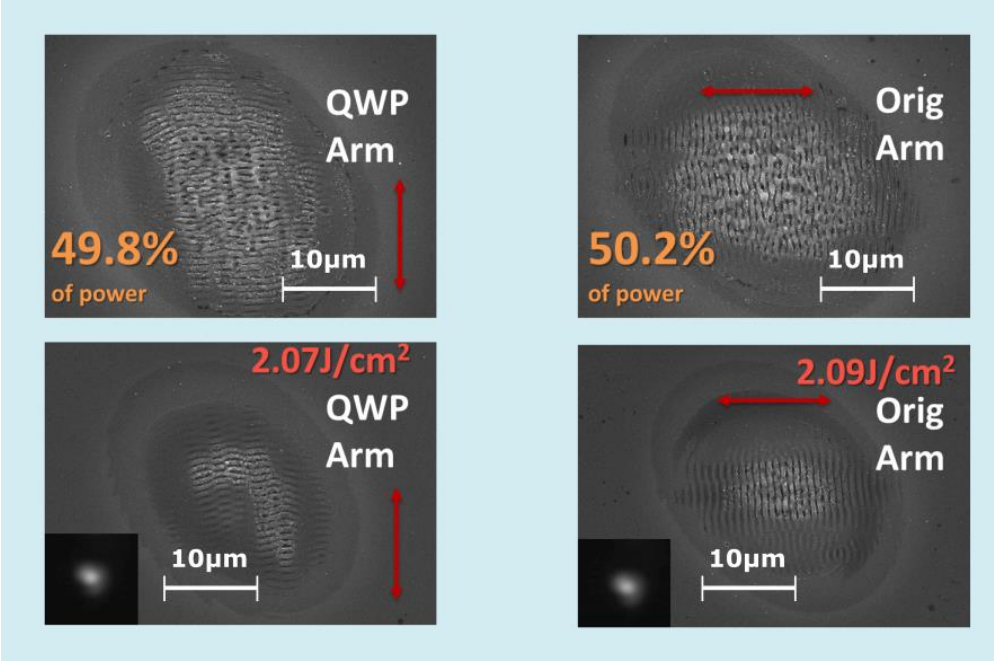

Figure 4.1 Result of the irradiation of single arms (QWP & Or.A as described in 3.2.1) (SEM images)

As it was described above, the inevitable inequality of energy distribution between the two arms is conspicuous for fluences near the damage threshold (two images below in Figure 4.1). Nonetheless that fact does not prohibit us to observe a few, very interesting, delay dependent phenomena in silicon. Inserted in the bottom SEM images of Figure 4.1 is the beam profile (obtained with a CMOS camera) at the focal point for each separate arm.

4.1.1 Large Delays (±50ps)

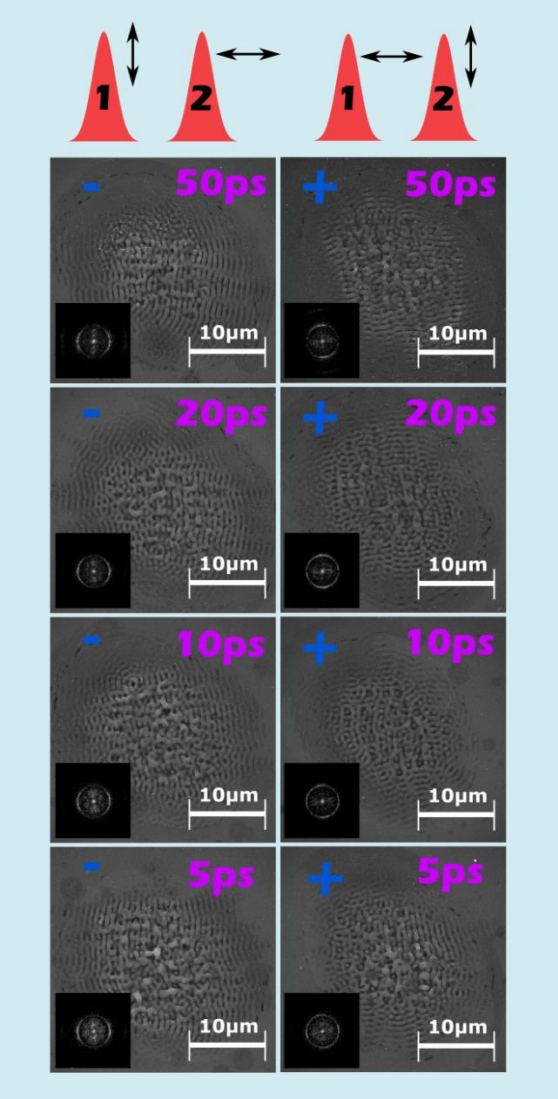

Figure 4.2 Silicon surface irradiated at large delay regime (SEM Images)

In this part we present the data that represent the timescale above the Phonon relaxation time (measured to last a few picoseconds[36]) (Figure 4.2) and during the thermalization of the material[1 11]. At this region the electrons have reached thermal equilibrium with the lattice. Electron population in the conduction band and the surface is still high[12] and the reflectivity progressively rises from 2ps to 50ps[37], [38]. This procedure occurs due to the temperature of the silicon surface which at that time has surpassed the 3000K and which exhibits metal behavior1. A predominance of the ripples that are created from the second pulse is observed for time delays up to 50 ps. The leading pulse is responsible for the less predominant ripples. This is observed in both the SEM images (Figure 4.2) and in Graph 1 Also there is a step in times close to 0ps during which ripples in both directions change period (Graph 1).

In the Figure 4.2 the 2D FT are result of averaging 13 iterations.

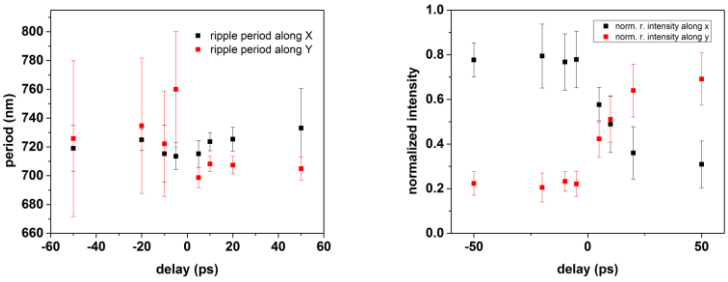

Graph 1 large Delays: Ripple period and frequency intensity evolution

4.1.2 Intermediate Delays (±2ps)

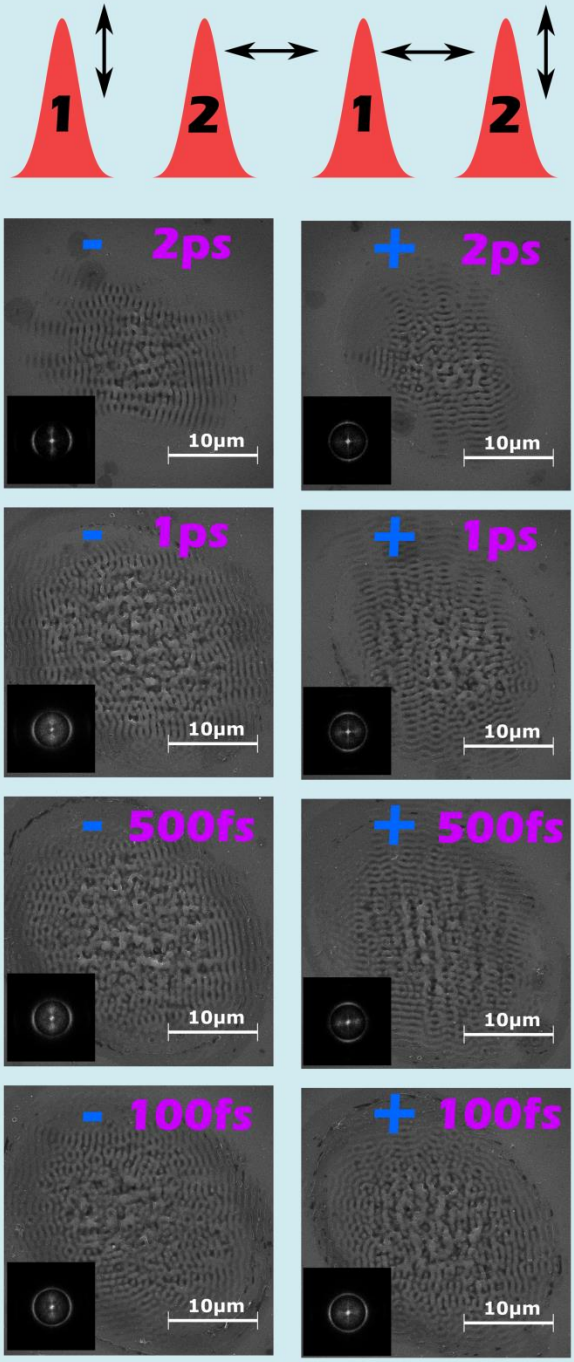

Figure 4.3 Silicon surface irradiated at Intermediate Delay Regime (SEM Images)

In this delay scale that varies between 0ps and 2ps the electrons exited by the fist pulse haven't yet equilibrate with the lattice when the second pulse arrives on the surface[1]. In this part electron phonon coherence may be responsible for the resulting nanostructure[36].

For delays above 500fs the predominance of the ripples of the second pulse is observed also, as it lager delays (Figure 4.3 & Graph 2).

The observed reduction of the nanostructured area in this timescale can be related to the reduction of the SPP [39] active area respectively with time which yet seems to increase again for delays larger than 5ps as it is shown in Graph 3.

Another interesting observation is that the nanostructure changes radically from 100fs to 500fs.In 100fs images there is no clear predominance of a ripple orientation axis, this indicates that a kind of entanglement can occur for such delays. This phenomenon will be further discussed in the next paragraph (4.1.3) in which small delay regime is examined.

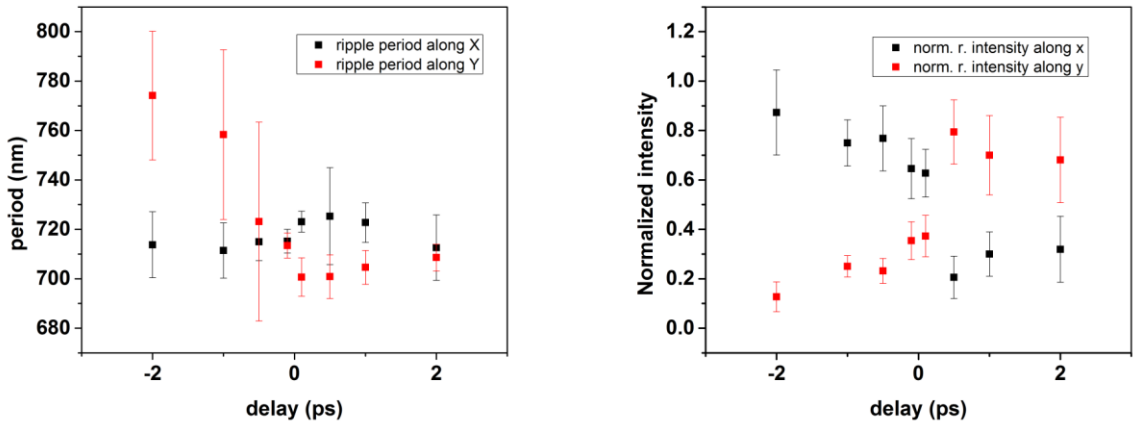

Graph 2 Shift of ripple period and intensity respectively to the row that the crossed polarized pulses reach the surface

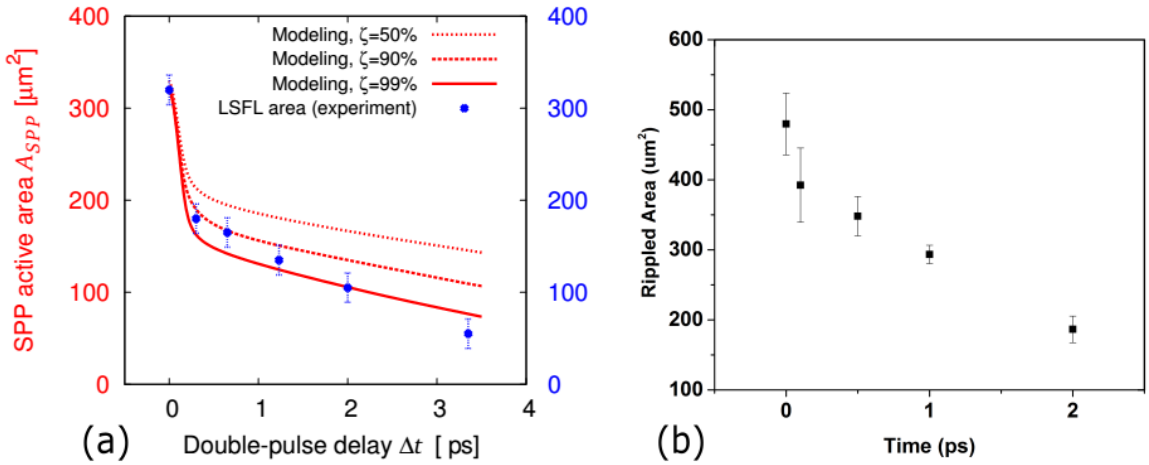

Graph 3 Reduction of SPP active area (image taken from Derrien et al.38) (b) measured nanostructured area

4.1.3 Small Delays (±260fs)

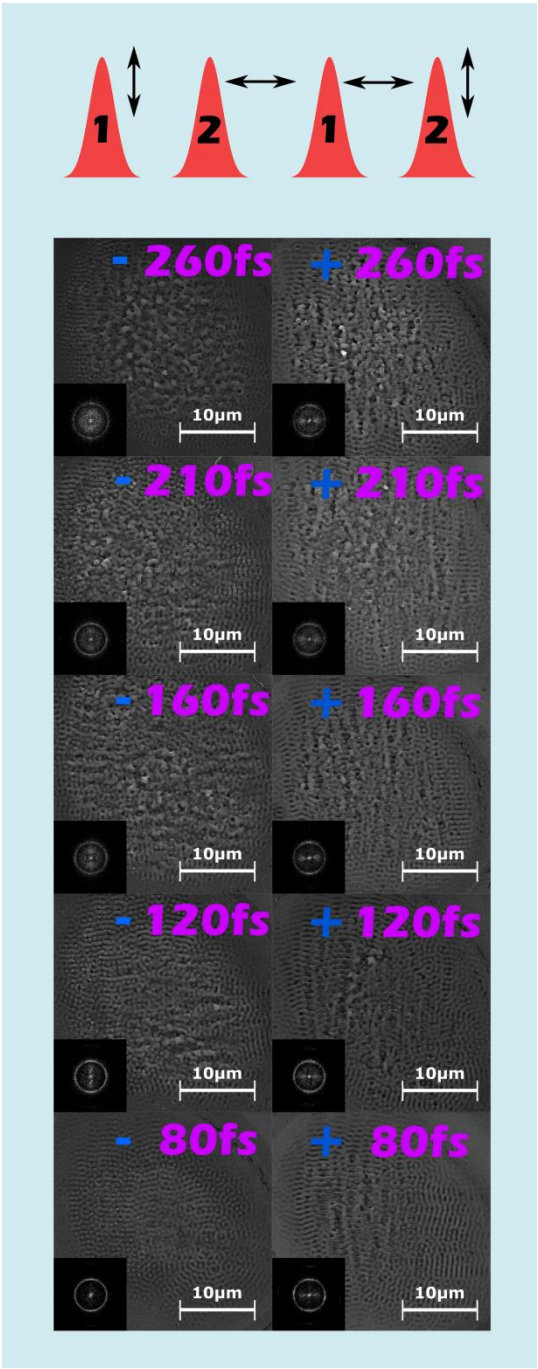

Figure 4.4 Small delays

In this part we examine the electron coherence effect on the LIPPS morphology. This coherence has a characteristic timescale smaller than 100fs in semiconductors[40].

The field correlation was measured to last (FWHM) from -40fs to 40fs. Thus the ±80fs represents approximately a 40 fs absence of irradiation between the pulses. The correlation time between the two pulses was measured as described in Paragraph 3.2.2.

With a careful observation of the SEM images shown in Figure 4.4, a progressive change of the presented nanostructure occurs from times ± 80 to ±160fs. This time delay window covers the delays before and after the overlap of the two pulses. The observed nanostructure in times smaller or around 100fs (±80fs and ±120fs) have a qualitative and quantitative difference than those in bigger delays. LIPPS formation is better defined in shape if not in direction as it shown in the 2D FT images (inset). Also the frequency noise that is seen in the images and 2D FT of larger delays faints as we approach the overlap of the pulses.

The fact that ripple morphology has a circular symmetry may indicate that the proposed for the ripple formation SPP's, created by the two subsequent pulses are overlapping in time delays where the two pulses do not. This does not opposes the bibliographical description of electron coherence, which was measured to last ~40fs in GaAs [40].

The certainty for the disentanglement of the electric fields of the pulses comes both from cross- correlation measurements as from the fact that the LIPPS nanostructure has a clear axial symmetry when the fields overlap as it was shown in Figure 4.5. For zero time delays the two fields are added to create a linear polarized pulse with orientation in between the axes of polarization of the two pulses.

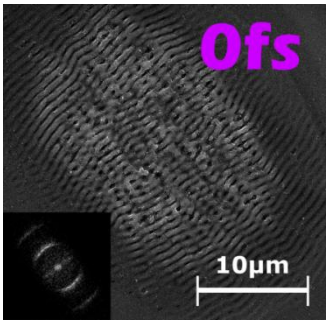

Figure 4.5 Nanostructure morphology at zero delay (SEM image). Inset: FT of the SEM image

The expected morphologies near the pulse overlap region are shown schematically below (Figure 4.6):

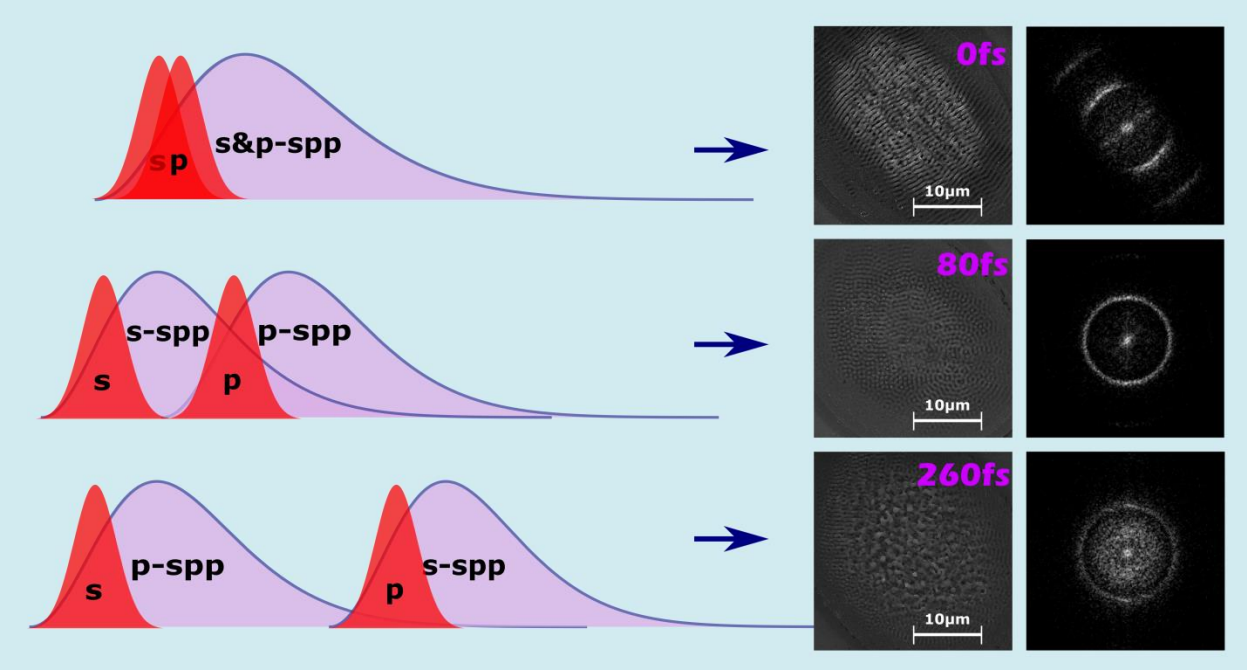

Figure 4.6 SPP overlapping

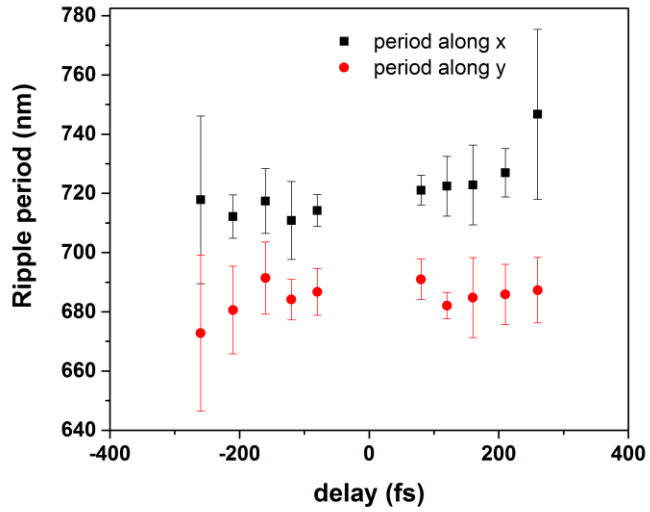

Graph 4 Small Delays - Ripple period

In Graph 4 ripple periodicity measurements along both polarization axes are presented. Error bars are derived from the standard deviation of five repetitions of the experiment in each delay:

Different periodicities along the axes Y and X in this case, are connected to unequal distributions in the fluences of the two pulses. This observation is much more intense in Paragraph 4.2 in which two pulses with fluence ratio 2:1 were implemented to irradiate the surface.

4.1.4 Phase Delay

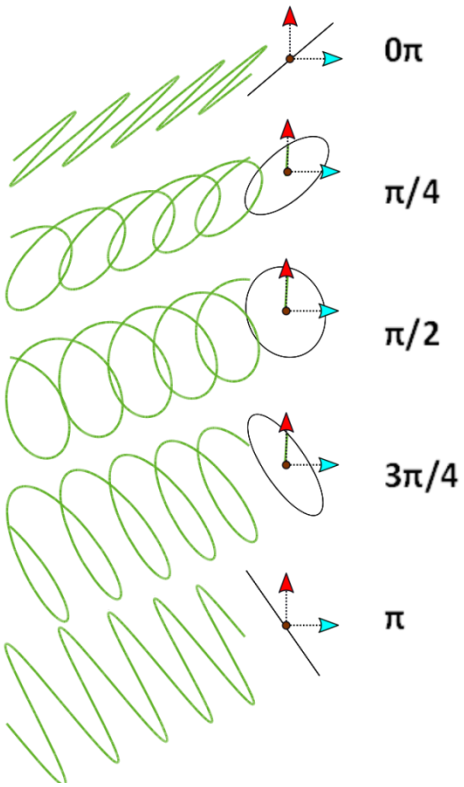

Figure 4.7 Graphical representation of Field addition as a function of the phase difference between the Ex, Ey field components

In this part we examine the different morphologies that accrue from the phase delay between the two linearly polarized pulses. In Figure 4.7 we show a few examples of the outcome of the addition of two sinusoidal electric fields with various phase delays between them. Red and cyan vectors show the axes of the polarization of the two initial fields at phase delay 0. The phase delay region extends from 0 to π and each field corresponds to the labeled delay.

It has been observed in many materials, that ripples are formed perpendicular to the polarization, in the case of the linearly polarized pulse, and in the case of the elliptical polarization ripples come perpendicular to the ellipse bigger axis[41-43]. Based on the bibliography and in Figure 4.7 ripple formation must be oriented in two main axes, +45° and -45° reference to any of the two pulse.

In order to ascertain the eventual possibility to control ripple orientation by controlling the delay of two perpendicularly polarized pulses two linearly polarized pulses with controlled delay accuracy of ~0.2 fs were used. In order to calibrate the phase delay of the two pulses the characterization part of the setup (Par. 3.2.2) a G-T polarizer was placed as it is shown in Figure 3.4. After that, a cross correlation of the two pulses was performed in order to measure the intensity of the field that past the G-T Polarizer in consecutive delays. The result of this measurement is show in Figure 4.8.

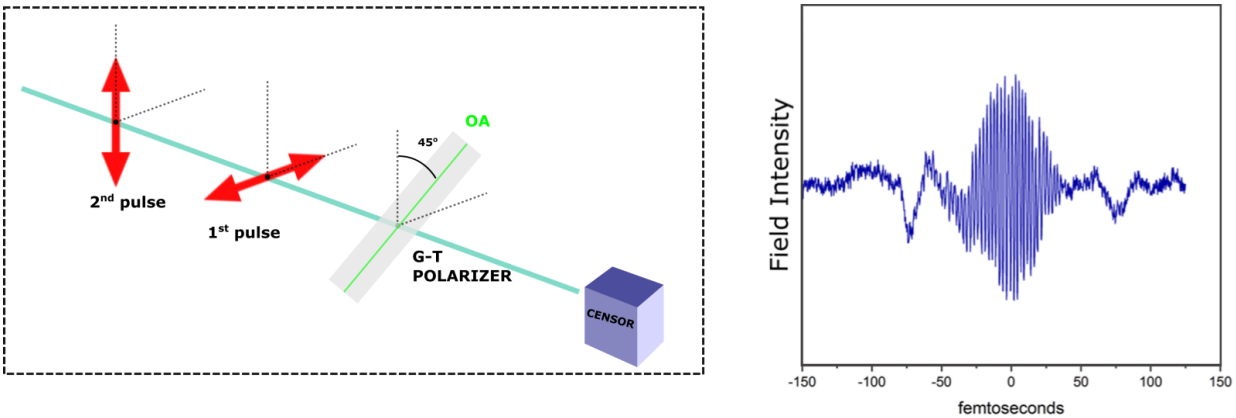

Figure 4.8 Field Correlation Measurement

The principle of this measurement (Figure 4.8) is quite simple. If we make the assumption that the two pulses are linearly polarized and the polarization is vertical in between them, then each peak of the field during the measurement means that the addition of the field results in a linearly polarized pulsed the direction of which is parallel with the OA of the G-T polarizer. Each valley represents a resulting pulse that is polarized perpendicularly to the OA of the G-T polarizer.

Figure 4.9 shows a zoomed area of the previous measurement (Figure 4.8). Measured field intensity is the black line and the fitted sinusoidal function is marked with red dashed line. Between the two dashed blue boarders lies the time delay window of the experiment. Seven successive time delays have been chosen to irradiate the silicon surface, inside that window, with delay step 0.5fs and accuracy 0.2fs. The results of the experiment are presented in Figure 4.10.

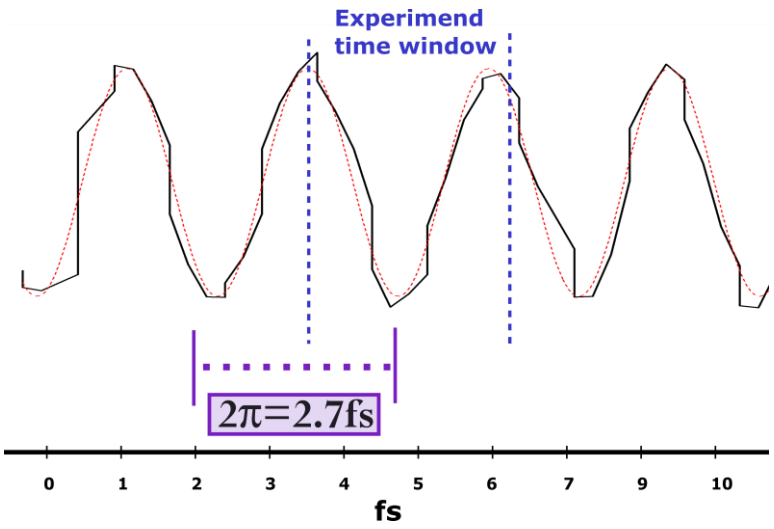

Figure 4.9 Field Measurement (zoom)

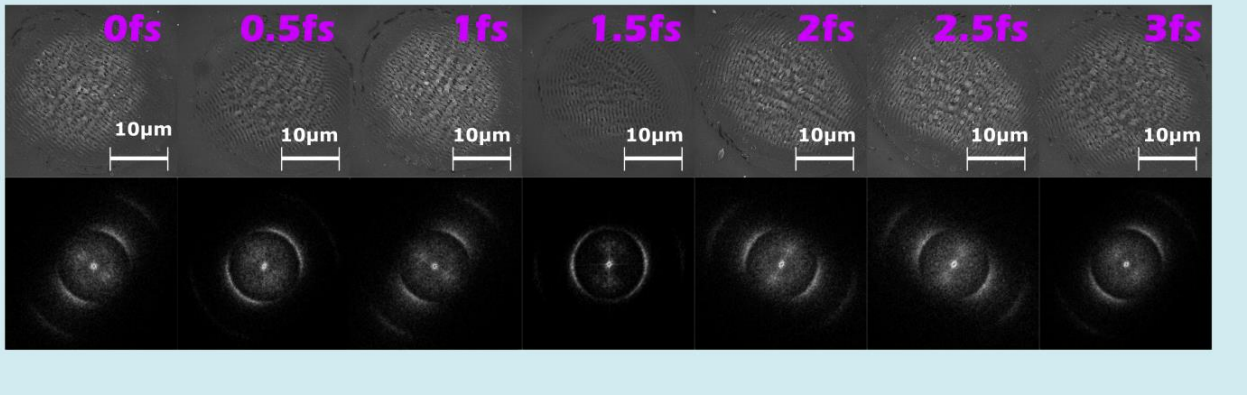

Figure 4.10 Ripple axis turn in respect to delay between the crossed polarized pulses (SEM images)

For each time delay, five iterations have been made in silicon surface. The 2D FFT that are shown in Figure 4.10 are the product of the averaging of five different images each of those 2D FFT images come from a different iteration. Even though the experimental errors that are related to the stage accuracy both in time delay and the small movement in each step that result in an angle displacement. By this measurement it is evident that ripple morphology can be also controlled threw delay conformation means.

The SPP overlapping is evident also from the absent of a significant change in the ripple periodicity respectively to the sequence that S&P polarized pulses reach the surface.

4.2 Pulses with unequally distributed energy

Here we present another observation related to LIPPS formation. Fluence influence. The basic aim of this experiment was to prove that despite which pulse arrives second the ripple nanostructure is defined by the pulse with the higher fluence. In order to do that I used a suitable filter to reduce the fluence of one arm of the modified autocorelator discussed in Paragraph 3.2.1. The resulting nanostructure of single arm irradiation with two pulses is presented in the figure below:

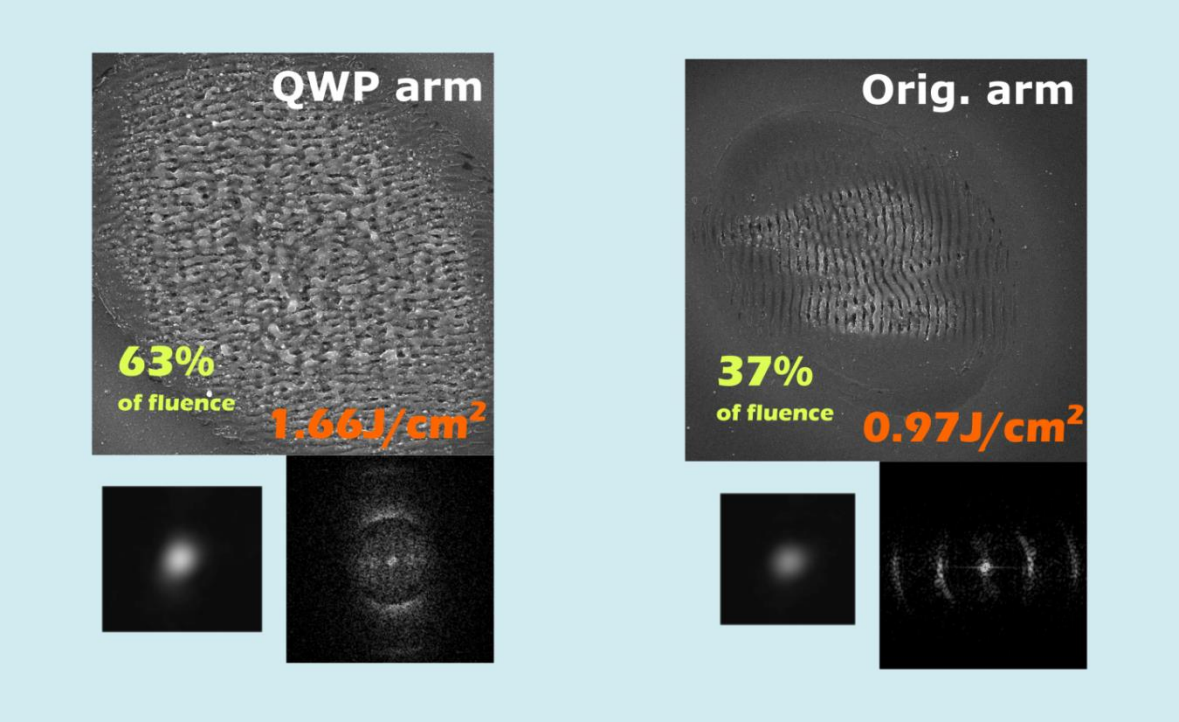

Figure 4.11 Result of the irradiation of single arms (QWP & Or.A as described in 3.2.1) (SEM images)

Inserted in Figure 4.11 the 2D FFT of each image and its beam profile.

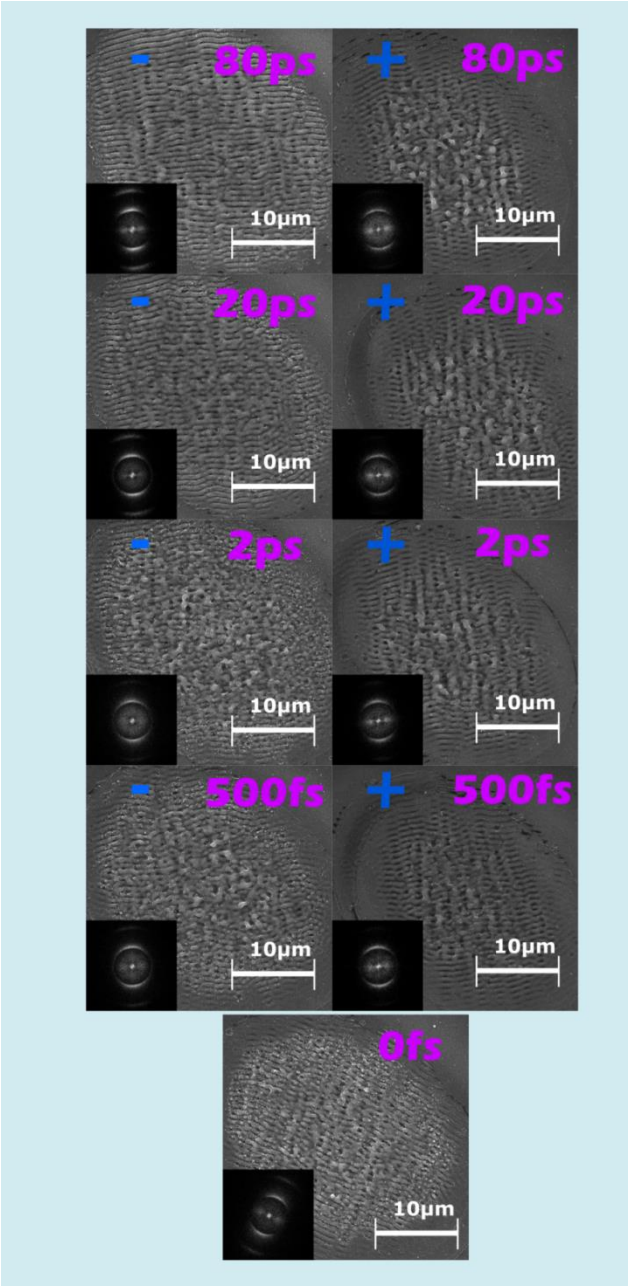

Figure 4.12 Resulting nanostructure in the case of pulses with Unequal distribution in fluence (SEM images)

The profound result which is presented in Figure 4.12 is the predominance of the LIPPS formation of the Pulse with the higher fluence, yet this is not the only interesting observation.

HF ripples are strongly present in the cases that the strongest pulse reaches the surface at least 20ps after the first. In in this time delays it seems that the interaction of the pulse with the surface is more efficient.

In Graph 5 we see that when a pulse arrives first the ripples that are created have lower intensity in the 2D FT compared to the case in which it comes second. This shift occurs progressively in time delays about -20ps to +20ps. After that delay region, ripple formation intensity is stabilized. In negative delay region the presence of ripples along the x axis was so dim that there could not be an accurate measurement of their period.

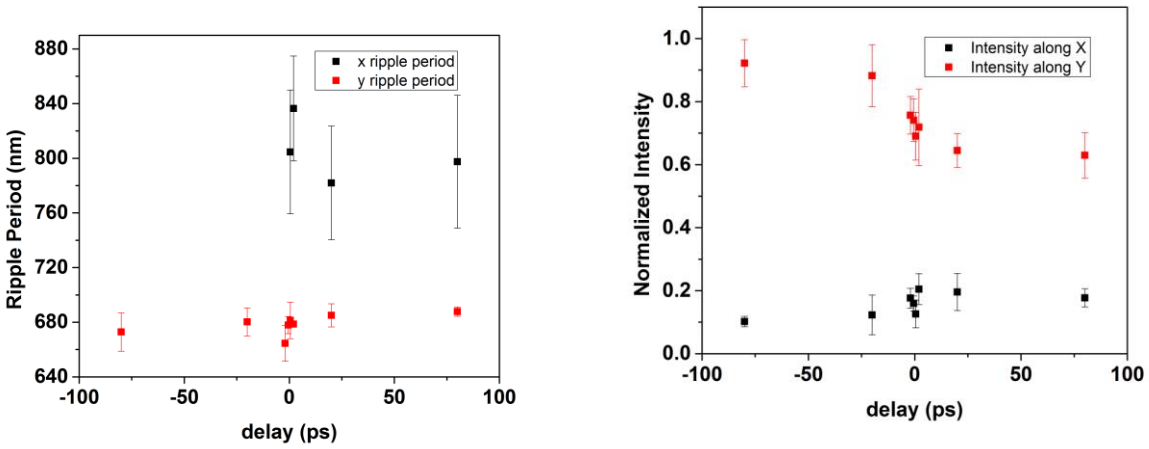

Graph 5 Ripple Period and Normalized intensity

The same deduction comes also from the examination of the diagram in Graph 6 for the HF ripples observed in the SEM images. In this case also the second pulse seems favored in ripple formation impact.

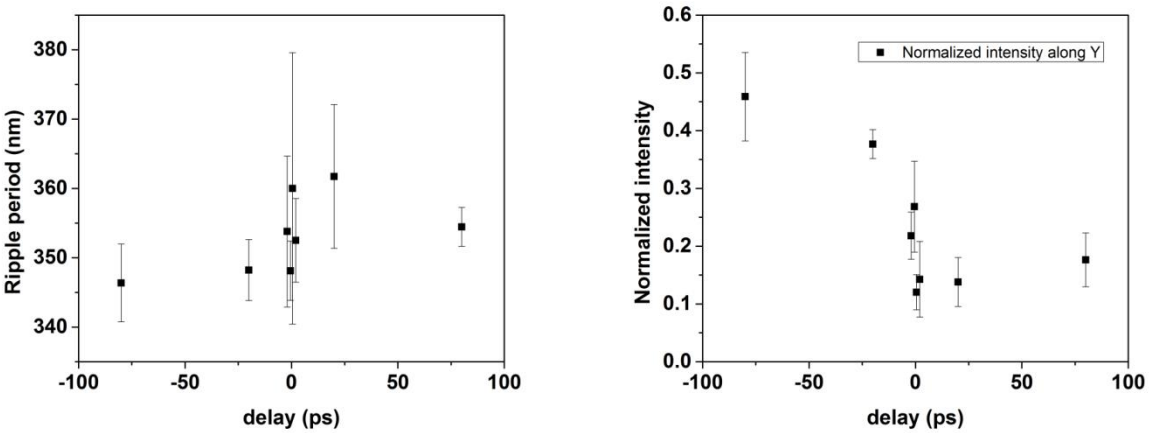

Graph 6 HF Ripple Period and normalized intensity

5 Conclusions:

Summarizing the results of the presented experiments, the first thing that has to be noted is that silicon surface after double, crossed polarized, pulse irradiation exhibits altered morphology depending on the delay. More specific the response of the surface can be categorized in four delay regimes based on the predominant interaction mechanism in each regime.

- Pulse overlapping regime, in which the fields of the two crossed polarized pulses overlap
- Delays from 0fs to 200fs during which surface plasmon interactions take place
- Delays below 100fs to 2ps in which electron phonon interactions take place
- Delays 5ps to 50ps in which the material exhibits metal behavior

In the case of two sets of two crossed polarized pulses the following major observations have been made:

- In delays larger than ~100fs there is a predominance of the nanostructure induced by the second pulse (Figure 5.1)
- There are two regions in the nanostructure area. The center in which there is a sort of chaotic nanostructure and the outer region in which ripples are formed. (Figure 5.1)

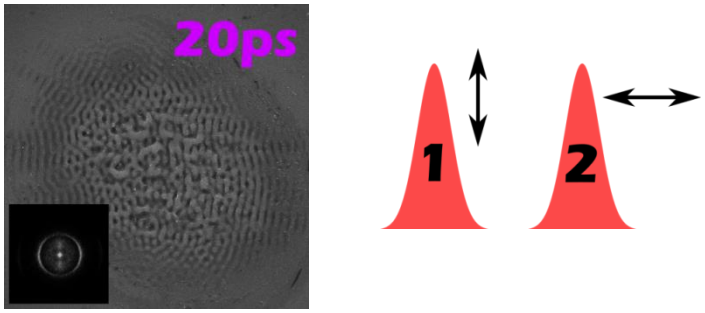

Figure 5.1

- Ripple periodicity changes as the row of the pulse changes. This applies both for LF and HF ripples (if those are present). The first pulse makes ripples with larger period compared to the second. (Graph 1 Graph 4 Graph 6)
- Ripple period and Frequency intensity in 2D FT diagrams are inversely proportional values in all cases (equal & non- equal distributed pulses). (Graph 1 Graph 4 Graph 6)
- For delays 500fs to 2ps the predominance of the second pulse is most evident compered to larger delays.

- In delays between ±500fs and ±2ps there is a reduction of the nanostructured area and this can be related to the SPP active area upon double pulse irradiation based to the bibliography[39] (Graph 3)
- In delays ±260fs there is a radical change in the morphology of the surface (Figure 4.6) from 45^{O} axis ripples to a new nanostructure with circular symmetry and after to a chaotic nanostructure.
- For "zero" delays, namely for phase retardation of the electric fields of the two pulses it is possible to rotate the ripple symmetry axis from -45^{o} to +45^{o} in few femtosecond delays (Figure 5.2).

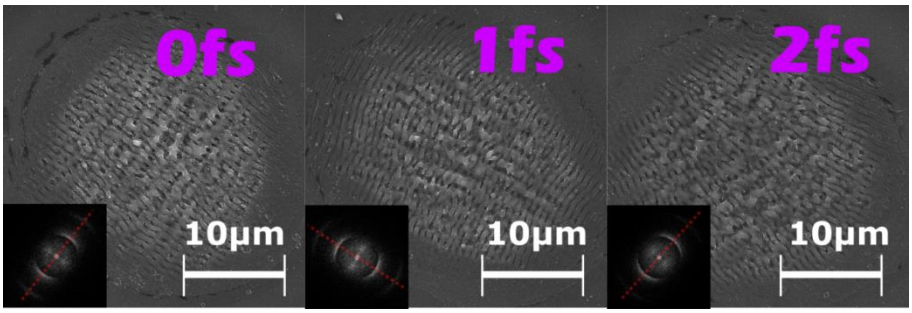

Figure 5.2

- For zero time delay between the two pulses the nanostructure that is observed is the imprint of the summation of the field of the two pulses.

In contrary to observations in dielectrics[8], in silicon the second pulse is the one that defines the ripple orientation. The fact though, that the pulse with the higher fluence defines the ripple formation and suppresses the lower pulse's influence in ripple formation is enhanced is silicon to the point that a 2:1 ratio in pulse fluence distribution is sufficient to overshadow the ripple formation by the lower fluence pulse as it is presented in Paragraph 4.2.

Threw the examination of the experimental part, one could not note the great possibilities that temporal pulse shaping has to offer. In this work we examine a small part of the possible applications of this technique in semiconductors. Different kind of materials, such as ceramics polymers and dielectrics exhibit a qualitative different response to femtosecond pulse irradiation. Temporal pulse shaping and polarization shaping could be the key to treat this kind of materials which are used in various application in order to enhance their operation.

Acknowledgments

I would like to express my gratitude to my supervisor P.A. Loukakos, for his constant presence and guidance during the implementation of this work as well as for his teachings. Furthermore, I would like to thank Dr. E. Stratakis, for his contribution to the overall planning and his motivation. Ms. A. Manoysaki for the hours spend in SEM characterization, V. Skoulas for his aid and encouragement and D. Karanikolopoulos for his theoretical and practical assistance during the experimental process.

References

1. G. D. Tsibidis, M. Barberoglou, P. A. Loukakos, E. Stratakis and C. Fotakis, Physical Review B **86** (11) (2012).

2. A. Y. Vorobyev and C. Guo, Laser & Photonics Reviews **7** (3), 385-407 (2013).

3. V. Zorba, E. Stratakis, M. Barberoglou, E. Spanakis, P. Tzanetakis, S. H. Anastasiadis and C. Fotakis, Advanced Materials **20** (21), 4049-+ (2008).

4. A. Y. Vorobyev and C. L. Guo, Applied Physics Letters **94** (22), 3 (2009).

5. A. Y. Vorobyev and C. Guo, Journal of Nano Research **14**, 57-67 (2011).

6. G. D. Tsibidis, C. Fotakis and E. Stratakis, Physical Review B **92** (4), 6 (2015).

7. M. Barberoglou, D. Gray, E. Magoulakis, C. Fotakis, P. A. Loukakos and E. Stratakis, Opt Express **21** (15), 18501-18508 (2013).

8. M. Rohloff, S. K. Das, S. Höhm, R. Grunwald, A. Rosenfeld, J. Krüger and J. Bonse, Journal of Applied Physics **110** (1), 014910 (2011).

9. S. Höhm, M. Rohloff, A. Rosenfeld, J. Krüger and J. Bonse, Applied Physics A **110** (3), 553-557 (2013).

10. S. Höhm, M. Herzlieb, A. Rosenfeld, J. Krüger and J. Bonse, Applied Surface Science **336**, 39-42 (2015).

11. S. K. Sundaram and E. Mazur, Nat Mater **1** (4), 217-224 (2002).

12. J. R. Goldman and J. A. Prybyla, Physical Review Letters **72** (9), 1364-1367 (1994).

13. H. M. v. Driel, PHYSICAL REVIEW B (1987).

14. H. K. a. M. Rinker, PHYSICAL REVIEW B (1992).

15. J. P. Long, H. R. Sadeghi, J. C. Rife and M. N. Kabler, Physical Review Letters **64** (10), 1158-1161 (1990).

16. E. Leveugle, D. S. Ivanov and L. V. Zhigilei, Applied Physics A **79** (7), 1643-1655 (2004).

17. C. Wu and L. V. Zhigilei, Applied Physics A **114** (1), 11-32 (2013).

18. C. N. A. J. Solis, J. F. Trull, and M. C. Morilla, J. Appl. Phys (1994).

19. Y. S. E. N. Glezer, L. Huang, and E. Mazur, PHYSICAL REVIEW 8 (1995).

20. Z. Haiyan, N. Wenchong, Z. Bin, L. Yongping, K. Masaru and I. Takashi, Journal of Physics D: Applied Physics **44** (48), 485302 (2011).

21. C. Jung-Ho, F. F. Dave, O. M. John and J. H. Kendall, Journal of Physics D: Applied Physics **42** (17), 175502 (2009).

22. J. E. Sipe, J. F. Young, J. S. Preston and H. M. van Driel, Physical Review B **27** (2), 1141-1154 (1983).

23. T. J.-Y. Derrien, T. E. Itina, R. Torres, T. Sarnet and M. Sentis, Journal of Applied Physics **114** (8), 083104 (2013).

24. M. Huang, F. Zhao, Y. Cheng, N. Xu and Z. Xu, ACS Nano **3** (12), 4062-4070 (2009).

25. N. M. Bulgakova, R. Stoian, A. Rosenfeld, I. V. Hertel, W. Marine and E. E. B. Campbell, Applied Physics A **81** (2), 345-356 (2005).

26. N. R. Isenor, Applied Physics Letters **31** (3), 148-150 (1977).

27. A. M. Weiner, Review of Scientific Instruments **71** (5), 1929-1960 (2000).

28. R. Stoian, M. Boyle, A. Thoss, A. Rosenfeld, G. Korn and I. V. Hertel, Applied Physics A **77** (2), 265-269 (2003).

29. M. Baeumler and R. Haight, Physical Review Letters **67** (9), 1153-1156 (1991).

30. M. Barberoglou, G. D. Tsibidis, D. Gray, E. Magoulakis, C. Fotakis, E. Stratakis and P. A. Loukakos, Applied Physics A **113** (2), 273-283 (2013).

31. T. Brixner, G. Krampert, P. Niklaus and G. Gerber, Applied Physics B **74** (1), s133-s144 (2014).

32. S. Rützel, A. Krischke and T. Brixner, Applied Physics B **107** (1), 1-9 (2012).

33. J. Bonse, J. Krüger, S. Höhm and A. Rosenfeld, Journal of Laser Applications **24** (4), 042006 (2012).

34. A. Borowiec and H. K. Haugen, Applied Physics Letters **82** (25), 4462-4464 (2003).

35. R. Le Harzic, D. Dörr, D. Sauer, F. Stracke and H. Zimmermann, Applied Physics Letters **98** (21), 211905 (2011).

36. M. Hase, M. Kitajima, A. M. Constantinescu and H. Petek, Nature **426** (6962), 51-54 (2003).

37. J. M. Liu, H. Kurz and N. Bloembergen, Applied Physics Letters **41** (7), 643-646 (1982).

38. A. J. Sabbah and D. M. Riffe, Physical Review B **66** (16) (2002).

39. T. J. Y. Derrien, J. Krüger, T. E. Itina, S. Höhm, A. Rosenfeld and J. Bonse, Opt. Express **21** (24), 29643-29655 (2013).

40. Shingo Hayashi1, Keigo Kato1,2, Katsura Norimatsu1,2, Masaki Hada1,3, Yosuke Kayanuma1,2 and & Kazutaka G. Nakamura1, SCIENTIFIC REPORTS (2014).

41. J. Yang, R. Wang, W. Liu, Y. Sun and X. Zhu, Journal of Physics D: Applied Physics **42** (21), 215305 (2009).

42. Y. Tang, J. Yang, B. Zhao, M. Wang and X. Zhu, Opt. Express **20** (23), 25826-25833 (2012).

43. W. Han, L. Jiang, X. Li, P. Liu, L. Xu and Y. Lu, Opt Express **21** (13), 15505-15513 (2013).